CONFIDENTIAL

The assessment of aerodynamic interaction between VentiFoil suction wings

A comparison between a numerical lifting line approach and full-scale RANS simulations

M. N. Borren

Master of Science Thesis

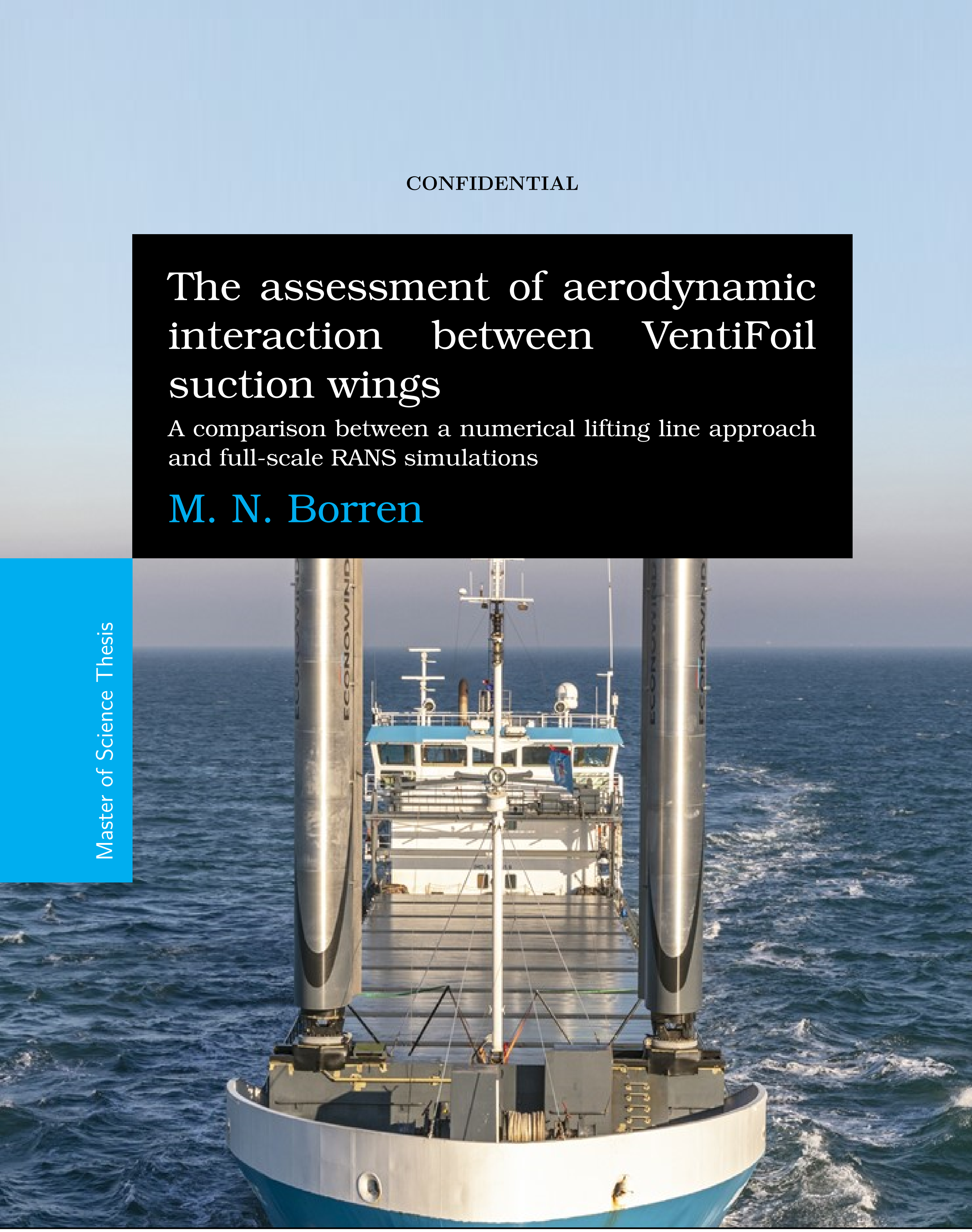

TU Delft
Delft University of Technology

MSc Marine Technology - Ship Hydromechanics

The assessment of aerodynamic interaction between VentiFoil suction wings

A comparison between a numerical lifting line approach and full-scale RANS simulations

For the degree of Master of Science in Marine Technology in the specialization of Ship Hydromechanics at Delft University of Technology

By

M. N. Borren

Performed at

Maritime Research Institute Netherlands (MARIN)

This thesis MT.21/22.025.M. is classified as confidential in accordance with the general conditions for projects performed by the TU Delft.

April 5, 2020

Company supervisors
Responsible supervisor: R. Eggers
E-mail: r.eggers@marin.nl
Daily Supervisor: J.J.A Schot
E-mail: j.j.a.schot@marin.nl

Thesis exam committee
Chair: T.J.C. van Terwisga
member: A.A. Kana
member: C.H. Thill
Company member: R. Eggers
Company member: J.J.A. Schot
Company member: F. Nieuwenhuis

Author details
Studynumber: 4298403
Author contact e-mail: marcborren@hotmail.com

The realization of this definition study has been made possible by Maritime Research Institute Netherlands (MARIN). Additionally, the work presented in this thesis was supported by eConowind. Their cooperation was very valuable and is hereby gratefully acknowledged.

Copyright © Marine Technology
All rights reserved.

Abstract

While the awareness of global warming rises, transport over sea remains a large contributor to green house gas emissions. New regulations imposed by the International Maritime Organization (IMO) aim to reduce the emission of green house gasses. Consequently, ship owners turn to technological solutions in order to achieve this. The Ventifoil from Econowind is a promising device in the field of Wind Assisted Ship Propulsion (WASP). By applying boundary layer suction, this airfoil shaped profile can generate large aerodynamic forces, which are used as additional propulsion to reduce fuel consumption. Often multiple devices are installed on the deck of a vessel.

Literature shows that the aerodynamic interaction between multiple airfoils can significantly influence the local flow conditions in which each individual device operates. Nonetheless, literature agrees that it is possible to mitigate detrimental effects by adapting to the local conditions. The operational guideline of the Ventifoils are based on the far-field wind conditions. Consequently, aerodynamic interaction between Ventifoils is not considered. This leads to the main research question: "To what extend does aerodynamic interaction between two Ventifoils mutually affect aerodynamic performance?". This thesis aims to analyse aerodynamic interaction using a numerical Lifting Line Model (LLM). This method has the potential of evaluating a broad range of operational and environmental conditions in limited computational time.

Aerodynamic interaction between two Ventifoils will be evaluated over a range of apparent wind angles between 0° and 180°, for two different absolute distances. The results from the LLM will be validated by means of three dimensional, steady Reynolds Averaged Navier Stokes (RANS) simulations. Five different interaction components will be analysed, being; changes in flow angle, changes in flow velocity, viscous interaction, pressure field interaction, and boundary layer suction interaction.

The results reveal that aerodynamic interaction can reduce the lift and drag coefficients by multiple tens of percentages. It is found that the reduction ratio of the thrust force coefficient, C_X, varies between -16% and -1% relative to a single isolated Ventifoil. The magnitude is mainly depending on the relative position of the devices. It is concluded that the interaction is most significant if the devices are positioned closely near each other and parallel to the flow direction. Both methods show good qualitative agreement. It is concluded that discrepancies in the magnitude of reduction ratios can be attributed to modelling differences in terms of viscosity, pressure fields and boundary layer suction. Better quantitative agreement is found for larger absolute distances. The LLM is furthermore used to maximize C_X by optimizing the angle of attack of each Ventifoil independently. The resulting increase in C_X showed to be between $+5\%$ and $+11\%$ added to the non-optimized reduction ratio.

Table of Contents

List of Figures

List of Tables

Acknowledgements

As a final act of commitment in obtaining my master's degree in ship hydromechanics, I present this research thesis. The final months were an effort where the objective was to implement the accumulated level of skill in engineering, physics, research, project management and other skills gained in the antecedent educational years. I have enjoyed being in charge of my own research, and look back with pleasure on the moments where analyses led to results and conclusions. It even made me consider proceeding in the field of academic research, something I had not considered before.

Although the subject and contents of the research were my own responsibility, I've enjoyed the guidance of several experts. Their critical view on the presented work were the basis of interesting discussions, which motivated and supported me throughout the project. My gratitude goes out to Rogier Eggers and Joost Schot, who have acted as my main supervisors during the entire project. Both assisted me on setting out the project scope and Lifting Line Model. Their input in topic related discussions and feedback was of much value to the contents of the report. Also I want to express my appreciation to Maxime Garenaux, which gave significant support setting up and processing the CFD simulations. Furthermore, I want to thank Frank Nieuwenhuis from Econowind for providing detailed information on the Ventifoil system and participating in the discussions. His experience added practical value to the results of the research. I want to thank Laurens-Jan Lagendijk on the various lunch time discussions on airfoil aerodynamics. As an Econowind employee and graduate on Ventifoil systems he gave me very useful advice in the field of the aerodynamic analyses. Finally, I want to express my appreciation to Tom van Terwisga for giving me feedback and advice on the definition study and the progress and results of this research.

I would also like to seize the opportunity to thank my parents, Jacob and Alexa, who have been of never diminishing support throughout my study, expressing their confidence when progress was moderate. I also want to express my appreciation to Laurien, for being patient and supportive during the times when I was preoccupied by study related work.

Delft, University of Technology M. N. Borren
April 2, 2022

Chapter 1

Introduction

Before the 20th century, ship propulsion was mainly provided by wind. With the development of the steam and fossil fuel engines, wind propulsion was becoming less and less necessary and remained only the primary propulsion for sailing enthusiasts. In the emerging necessity of emission reductions, the propulsion of ships using the wind is now again more relevant than before. Regulations designed by the International Maritime Organization (IMO) and enrolled by the Maritime Environment Protection Committee (MEPC), together with potential fuel savings, give ship owners and companies enough incentive to invest in systems which reduce energy consumption. Using the wind as additional propulsion source has shown large potential. It is for this reason, that Wind Assisted Ship Propulsion (WASP) has emerged in the past few decades. Many different devices are developed for WASP, of which most are based on generating aerodynamic lift forces. The aerodynamic forces are used as additional propulsive force, aiming to reduce fuel consumption.

Wind propulsors are often designed and optimized in controlled environments such as computational flow fields or wind tunnels. The performance of the device is then evaluated in undisturbed circumstances, for example isolated from the ship and other devices and with constant uniform wind profiles. However, the operational circumstances once installed on a ship are then not comparable to the circumstances used in the design stage.

The Ventifoil, developed by Econowind, is a promising wind propulsion device based on the Turbosail of Cousteau [3]. By using boundary layer suction, large aerodynamic forces can be generated by the devices. Often multiple devices are installed on the deck of a vessel, which leads to aerodynamic interactions between the Ventifoils mutually. Aerodynamic interaction can result in significant changes in local wind conditions. The definition study in the preamble of this research revealed that this can be detrimental for the generation of additional propulsive forces [9].

1-1 State of the art

The definition study showed that there are various ways to evaluate the behavior of multiple wind propulsors sharing a flow field [9]. It is common to use experimental methods such as wind tunnel tests. Sometimes also particle image velocimetry is used, which can visualize and quantify flow characteristics. This is for example done by [10] and [11]. However, these types of equipment and facilities can be expensive.

Many studies evaluate interaction with the use of two and three dimensional Computational Fluid Dynamics (CFD) simulations. Usually Reynolds Averaged Navier Stokes (RANS) methods are used [12, 13]. An advantage is that flow characteristics can be quantified and analysed with high accuracy [14]. For more time varying flow, Unsteady Reynolds Averaged Navier

Stokes (URANS) simulations offer a solution, this is for example used by [15]. For higher fidelity sometimes Large Eddy Simulations (LES) are used [16].

Recently, also the numerical implementation of analytical methods for the evaluation of wind propulsors is studied. Potential flow models based on the Lifting Line (LL) theory of Prandtl are for example compared with numerical or experimental results. There are multiple studies who try to asses aerodynamic interaction based on potential flow models [11, 17, 18]. The validity of the results differ, mainly caused by the introduction of modelling assumptions. None of these studies is focused on suction wings such as the Ventifoil.

1-2 Problem statement

The operational guideline of the Ventifoil is based on the far-field flow conditions, and does not operate on the conditions at the location of the Ventifoil itself. Econowind uses standardized settings, such as a constant, conservative angle of attack, which is equal for each individual Ventifoil. As a consequence, the aerodynamic interactions are omitted and the full potential of the devices might not be utilized. Evidently, there is need for a method which evaluates aerodynamic interaction between multiple Ventifoils.

The antecedent definition study has shown that the severity of aerodynamic interaction is dependent on environmental conditions and relative placement, i.e. the apparent wind angle and absolute distance between the devices. Furthermore, aerodynamic interaction depends on the operational configuration of the individual devices, e.g. the angle of attack [9]. All together the flow field resulting from aerodynamic interaction is a product of variables in a multidimensional, continuous design space. Finding a solution for a large range of possible combinations of variables is computationally challenging.

Solving and subsequently analysing the flow field under the influence of aerodynamic interaction is necessary in order to adapt and optimize operational guidelines. Unfortunately, methods are often expensive and time costly, which make them unsuitable for the evaluation of large design spaces. A method which can evaluate the broad range of configurations and conditions, with sufficient accuracy, without using much computational effort, is therefore needed to increase aerodynamic performance.

The lack of research on aerodynamic interaction between multiple Ventifoils leads to a knowledge gap on the extend of aerodynamic interaction and its effect on the performance of the system. This research will occupy this gap by answering the following research question:

- *To what extend does aerodynamic interaction between two Ventifoils mutually affect aerodynamic performance?*

With the following sub questions:

- *How can the aerodynamic interaction be modelled for practical, adaptive operation and improvement of aerodynamic performance?*
- *How are viscous and pressure field interactions involved in overall aerodynamic interaction?*

- *What is the effect of aerodynamic interaction on the suction coefficients and consequently aerodynamic performance?*

1-3 Method and scope

The research questions will be evaluated by means of a numerical Lifting Line Model (LLM). This method has the advantage of being computationally efficient and therefore allows for the evaluation of a large range of environmental and configurational settings. The method uses two dimensional aerodynamic properties of the Ventifoil as input. In order to obtain this, full scale two dimensional RANS simulations will be done. The output of the LLM will provide information on the aerodynamic coefficients and performance of each individual device. It will also provide insights in the local conditions at which the Ventifoils operate. Aerodynamic performance will be expressed in terms of the thrust force coefficient, C_X. After the implementation of the LLM, a method for adapting to the aerodynamic interaction in order to increase aerodynamic performance, will be presented.

The numerical LLM is based on the classical lifting line theory and consequently comes with limitations and assumptions. In order to validate the results, full scale three dimensional RANS simulations will be conducted both for a single Ventifoil, as for a configuration consisting of multiple Ventifoils. This will allow for the evaluation of interaction through pressure fields, viscosity and the effect of interaction on the boundary layer suction.

The model will be based on the geometry and properties of the Ventifoil following the latest developments. This way the focus will lay on varying operational en environmental parameters. In order to isolate the effect of aerodynamic interaction on the aerodynamic performance, the Ventifoils will be isolated from the ships hull on which they are normally mounted. This way the aerodynamic interference of the hull and superstructures, can be excluded from the results. Furthermore the study is limited to the aerodynamic properties of the devices. The hydrodynamics involved in WASP are left out of consideration.

The main objective of the research is to investigate the influence of mutual aerodynamic interaction on Ventifoil performance. This research aims to investigate the suitability of the LLM for evaluating aerodynamic interaction. The research furthermore aims to increase aerodynamic performance of the considered system by proposing adaptive operational guidelines.

1-4 Thesis outline

The second chapter of this thesis will elaborate on the working principle of airfoils, Ventifoils and will present a literature review on aerodynamic interaction. Chapter 3 will start with an overview on relevant fluid dynamics and continues with a detailed description of the modelling steps taken in the numerical lifting line approach and the RANS simulations. The results for the two dimensional RANS simulations will be presented in chapter A, which will function as the input data for the LLM. The evaluation of single Ventifoil aerodynamics, with a comparison between the LLM and RANS, will be presented in chapter B. After that, chapter C will elaborate on the effects of aerodynamic interaction between multiple Ventifoils. Multiple interaction components will be analysed extensively in order to validate the suitability of the

LLM for assessing aerodynamic interaction. Chapter D will present results on the aerodynamic performance of the benchmark configuration. Additionally, a method for adapting to interaction and its results will be presented. Finally, the research conclusions and further recommendations are given in chapter 5.

Chapter 2

Literature review

2-1 Wind Assisted Ship Propulsion

Wind Assisted Ship Propulsion (WASP) is used to propel the ship in a forward direction by harvesting wind energy in order to save fuel. The fact that this technology is referred to as *wind assisted* means that the goal is to assist the main propulsor of the ship; it's engine. This differentiates it from *wind propulsion.* It is of large importance that the main working of the ship is not hindered by the WASP devices [19].

2-1-1 Types of WASP devices

There are various devices which are used for the purpose of WASP. For example a wind turbine, can drive the propeller mechanically. However, most devices are based on generating an aerodynamic force, of which the forward directed component is used as additional thrust. There are multiple different devices which accommodate this. A well known example is the Flettner Rotor. This cylinder shaped device rotates around its vertical axis. Due to the Magnus effect a thrust force is produced. Kites are WASP devices which are flying above and forward of the ship. Furthermore there are soft sails and Dynarig installations which have a resemblance to traditional sailing rigging. A disadvantage of soft sails and Dynarigs is that in operation, view on cargo and surroundings of the vessel can be blocked due to the large area of the sails. Kites are very sensitive on being correctly manoeuvred in order to produce large thrust forces. Rigid wings are also a commonly used for the purpose of WASP and show large potential in head wind conditions. [19]

(a) Flettner rotors on the Maersk Pelican. *www.norsepower.com*

(b) Kite used as additional ship propulsion. *www.skysails-marine.com*

Figure 2-1: Two WASP configurations on commercial ships.

A promising wind propulsor is the Ventifoil from Econowind. This very thick airfoil with trailing edge flap has ventilation holes over which suction can be applied. If the airfoil, flap and suction are adjusted properly to the environment, it can generate large thrust forces. Multiple systems are already installed on different coastal trading vessels. Normally multiple Ventifoils are installed on a ship. An example of this is shown in the figure underneath.

(a) Ventifoils on the MV Ankie.

(b) Ventifoils on the MV Frisian Sea.

Figure 2-2: Ventifoil systems in operation. *www.econowind.nl*

2-1-2 Relevance for shipping industry

Over 90% of global trade is driven by shipping and this is on average responsible for 3.1% of global CO_2 emissions. It is stated by the International Maritime Organization (IMO) that CO_2 emissions in 2050 may be 90% to 130% of the emission level in 2008 [20]. In order to contribute to the deceleration of global warming, the IMO has ordered the Maritime Environment Protection Committee (MEPC) to propose a strategy to decrease the emission of Green House Gas (GHG). The initial goal was to decrease the annual emissions of GHG at least by 50% in 2050, compared to the emissions in 2008.

At the basis of the strategy developed by the MEPC stands technological innovation and the use of alternative fuels and energy sources. Part of the strategy is decreasing the CO_2 emission of ships by further enrolling the Energy Efficiency Design Index (EEDI) for new ships. The group of regulations described in the EEDI, incorporates multiple technological and operational requirements for newly build ships with a gross tonnage of 400 or higher [21]. It enforces that these ships are build based on a standard minimum level of energy efficiency. In February of 2017, over 2200 ships were given a certificate for following the EEDI [21]. The efficiency index is expressed in grams of CO_2 per tonne mile, were obviously a low rating corresponds to a high energy efficiency. The complete formula for calculating the EEDI of a ship is shown underneath.

The method also incorporates a reduction in EEDI rating if innovative technologies are installed. Such technologies are for example heat recovery systems, air lubrication systems, but also wind propulsion systems. The power which is generated or reused by such a device is included as 'available effective power'. For a wind propulsion device, this is the power being generated by the system. The term in which this is expressed is indicated by the red square. The available effective power is the product of the availability factor f_{eff} and the effective

$$EEDI = \frac{\left(\prod_{j=1}^{M} f_j\right)\left(\sum_{i=1}^{nME} P_{ME(i)} \cdot C_{FME(i)} \cdot SFC_{ME(i)}\right) + \left(P_{AE} \cdot C_{FAE} \cdot SFC_{AE}\right)}{f_i \cdot f_c \cdot Capacity \cdot f_w \cdot V_{ref}} + \frac{\left\{\left(\prod_{j=1}^{M} f_j \cdot \sum_{i=1}^{nPTI} P_{PTI(i)} - \sum_{i=1}^{neff} f_{eff(i)} \cdot P_{AEeff(i)}\right) C_{FAE} \cdot SFC_{AE}\right\} - \left(\boxed{\sum_{i=1}^{neff} f_{eff(i)} \cdot P_{eff(i)}} \cdot C_{FME} \cdot SFC_{ME}\right)}{f_i \cdot f_c \cdot Capacity \cdot f_w \cdot V_{ref}}$$

Figure 2-3: Energy Efficiency Design Index formula with red marking for wind propulsion contribution [1].

power P_{eff} [22]. As can be seen this results in a reduction of the EEDI rating. Specifically, the available effective power for wind propulsion is computed based on the equation below.

$$(f_{eff} \cdot P_{eff}) = \left(\frac{0.5144 \cdot V_{\text{ref}}}{\eta_T} \sum_{i=1}^{m} \sum_{j=1}^{n} F\left(V_{ref}\right)_{i,j} \cdot W_{i,j}\right) - \left(\sum_{i=1}^{m} \sum_{j=1}^{n} P\left(V_{ref}\right)_{i,j} \cdot W_{i,j}\right) \tag{2-1}$$

The first term is for the propulsive power contribution of the wind propulsion device. The factor 0.5144 is for the conversion of knots to meters per second. V_{ref} is the reference speed of the ship. η_T is the total propulsive efficiency of the main propulsor at 75% of the maximum continuous rating of the main engine, and is set as 0.7 if no value is specified. The term $F(V_{ref})_{i,j}$ is the thrust force matrix of the wind propulsor at V_{ref} for different apparent wind speeds and wind angles. $W_{i,j}$ is the global wind probability matrix, which is specified by the IMO [22].

The second term is the power which is consumed by the propulsion device in order to operate. For a suction wing, this will be the power which is needed by the fan to apply suction at the trailing edge of the wing. $P(V_{ref})_{i,j}$ is the power consumption matrix at V_{ref} for different apparent wind speeds and wind angles.

What can be concluded based on the equation for available effective power, is that the contribution of WASP to the EEDI is only based on the aerodynamic thrust force generated by the system. This means that possible additional hydrodynamic ship resistance caused by the operation of a WASP system, is not included in the calculations of the EEDI rating. However, the index is under constant development, and a renewed formula is expected to be presented next November. Therefor additional ship resistance due to wind propulsion might be included in future regulations.

2-2 Working principle of an airfoil

WASP often relies on devices which generate lift forces. The most commonly known lifting device is the airfoil. This chapter will elaborate on some basics principles and aerodynamic properties of airfoils.

2-2-1 Lift and drag

When either the trajectory or the velocity of fluid flow is diverted by the presence of an object, the momentum of the fluid particles has to be changed. This change in momentum is established by a conjunction of the object exerting a pressure on the fluid particles, and the fluid particles exerting a pressure on the object. This results in a pressure distribution over the surface of the object. Integrating the pressure over this surface results in a total force F_T, shown in figure 2-4. Drag is defined as the force component parallel to the incoming flow, whereas lift is defined as the force component perpendicular on the incoming flow [2]. A widely known lifting device is an airfoil, which is designed to generate large lifting forces. The forces on the airfoil can be rewritten as non-dimensional numbers, being the lift coefficient C_L and the drag coefficient C_D, shown in equation 2-2. Where F_L and F_D are the lift and drag forces, and A is the surface area of the airfoil. The use of these coefficients is very common and makes it possible to compare airfoils of different shapes and sizes.

$$C_L = \frac{F_L}{\frac{1}{2}\rho U^2 A} \tag{2-2a}$$

$$C_D = \frac{F_D}{\frac{1}{2}\rho U^2 A} \tag{2-2b}$$

For many applications, it is beneficial to generate as much lift as possible while at the same time maintain minimal drag. The ratio between the lift coefficient and the drag coefficient, $\varepsilon = \frac{C_L}{C_D}$, is often, but not always, referred to as the aerodynamic efficiency. The angle between the cord of the airfoil and the incoming flow is called the angle of attack, α. The lift and drag forces both generally increase with the angle of attack.

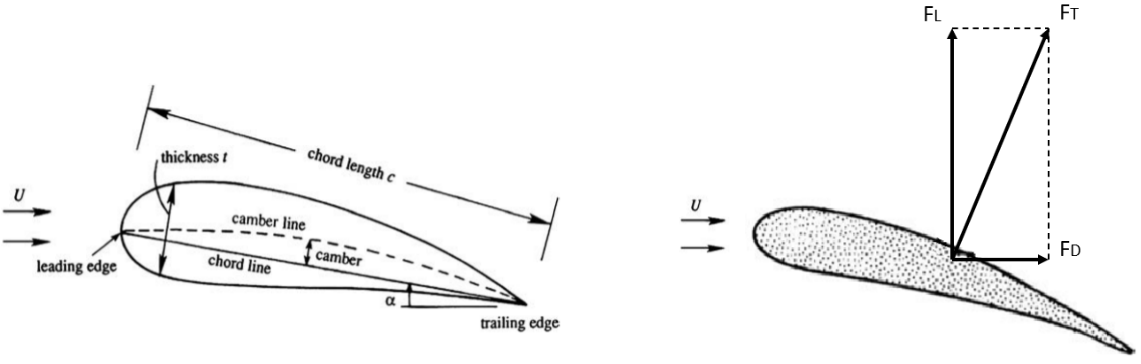

(a) Geometric definitions.

(b) Force decomposition.

Figure 2-4: The geometry and forces on an airfoil. [2]

2-2-2 Pressure distribution

In figure 2-5, a pressure distribution over the surface of an airfoil is given. For clarity, the y-axis has its negative values plotted above the x-axis. This pressure is often expressed as the non dimensional pressure coefficient C_P, shown in equation **??**.

$$C_P = \frac{p - p_{\text{inf}}}{\frac{1}{2}\rho U^2} \tag{2-3}$$

As can be seen, the origin of lift is mostly due to large negative pressures acting on the upper surface of the airfoil. The largest (negative) pressure peak lies just behind the leading edge on top of the airfoil. When moving further over the upper surface to the trailing edge, pressure increases, $\frac{\partial P}{\partial x} > 0$. This gradient is called an *adverse* pressure gradient. When the angle of attack increases, so does the magnitude of the low pressure region behind the leading edge. Consequently, the adverse pressure gradient also increases with the angle of attack. Because fluid is flowing from a low pressure region to a high pressure region, flow decelerates when moving towards the trailing edge.

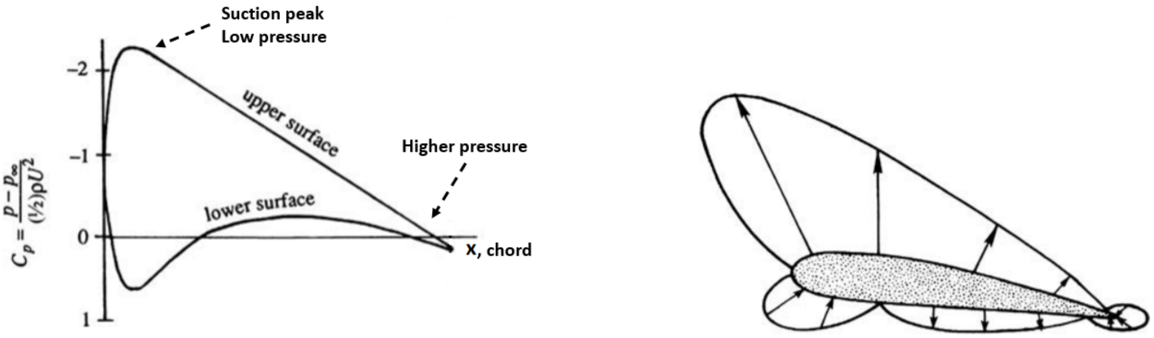

(a) Pressure distribution. **(b)** Orientation of normal stress on surface.

Figure 2-5: The pressure distribution and normal stress orientation on an airfoil section. [2]

2-2-3 Flow separation

The boundary layer is a flow region located on a surface, where the flow velocity is decreased due to surface friction. Because of the friction, the advection velocity gradually increases when moving in normal direction of the surface, the resulting velocity distribution is indicated with $U(x)$. An enlarged view of the upper surface of the airfoil, with a schematic representation of the boundary layer is shown in figure 2-6. Just behind the leading edge a low pressure peak is situated. This results in $\frac{\partial P}{\partial x} < 0$, and flow accelerates from the leading edge, towards this pressure peak. Directly after the minimum in C_P, the pressure gradient becomes adverse, resulting in a retardation of the advection velocity and thickening of the boundary layer [5]. At a certain point on the airfoil, the adverse pressure gradient is strong enough to reverse the direction of the flow just above the surface. The onset of this is called the separation point, indicated in figure 2-6 with an S. Since flow encounters S from both sides, a streamline indicated with I is directed away from the wall, i.e. the flow separates itself from the surface. The flow behind and under the separation streamline is called the wake. The surface pressure in the wake region is commonly much lower than the surface pressure at the leading edge. The differences between these pressures result in a (form) drag force on the body. It is for this reason, that C_D often takes on large values if the flow is separated.

The extend to which a boundary layer can withstand separation depends on the advection velocity of the boundary layer $U(x)$ and the magnitude of the adverse pressure gradient, $\frac{\partial P}{\partial x}$.

The latter, on its turn, depends on the curvature of the upper surface with respect to the incoming flow and on the angle of attack α.

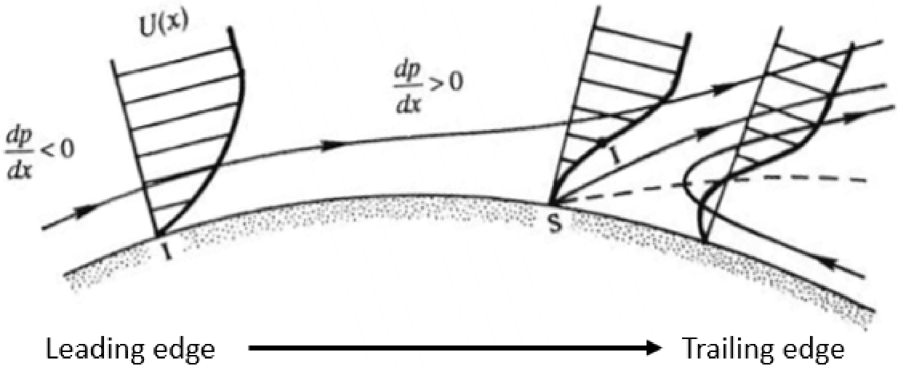

Figure 2-6: Schematic representation of boundary layer with adverse pressure gradient. [2]

For thick airfoils, the curvature of the leading edge will be smaller, the curvature of the trailing edge is often larger. Consequently, the suction peak is moderate, the adverse pressure gradient over the upper surface is smaller and flow will stay attached behind the leading edge and suction peak. If the curvature of the trailing edge is large, the adverse pressure gradient increases in that region and separation will occur towards the trailing edge. This is called trailing edge separation.

For slender airfoils, the curvature is large at the leading edge. This results in a substantial suction peak. The adverse pressure gradient behind the suction peak will be large and the onset of separation will be already behind the suction peak. However, for small α, the mean curvature over the entire upper surface can be moderate and separation can be prevented over the entire surface of the airfoil. Consequently, form drag on a slender airfoil can be small. If the flow separates at the leading edge, this can happen in broadly two manners. The flow can quickly reattach, there is only a small separation bubble at the leading edge and the flow remains attached over the rest of airfoil. If the flow does not reattach, and remains separated from the airfoil over its entire chord length, this leading edge separation will result in a large wake. Drag will then increase, while lift will decrease sharply. The airfoil is then in stall condition. [23]

As stated before, the angle of attack, α, has a large impact on the pressure distribution over an airfoil. In general, larger angles of attack will result in larger suction peaks. It is therefor common to plot the lift and drag coefficients as a function of α. A typical relation is shown in figure 2-7a. As can be seen, C_L and C_D increase over α. At certain α, the lift coefficient is at its maximum, C_{Lmax}. For higher angles, the adverse pressure gradient becomes to large, resulting in leading edge separation. The lift coefficient drops and drag increases due to the presence of a large wake. This is the earlier explained stall. The angle α at which this happens is the stall angle, α_{stall}. A schematic representation is given in figure 2-7b.

2-2-4 Aspect Ratio

Schematic representations often show a two dimensional section of a wing, but of course, airfoils are in reality three dimensional objects. As defined in 2D representations, there is a

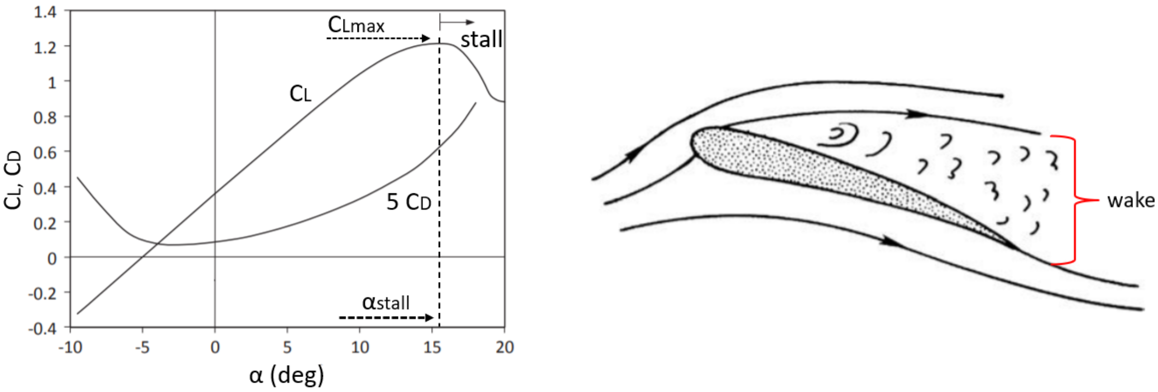

(a) Lift and drag coefficients.

(b) Airfoil in stall condition.

Figure 2-7: Airfoil characteristics over angle of attack α. [2]

pressure side and a suction side which stretches over the span of wing. Since the wing is of finite span s, fluid is moving around the edges from the high pressure side to the low pressure side. As is indicated in figure 2-8. The movement of fluid around the tips of the wing results in vorticity in streamwise direction, which convect with the flow. In the application of WASP this vorticity will therefor convect with the wind. As this vorticity is constantly generated, a continues vortex filament is convected away from the wing. This is called a tip vortex. Kinetic energy is continuously being fed to the tip vortex [2]. Consequently, this must be an additional drag for the wing. This drag force is oriented in the stream wise direction and is called induced drag.

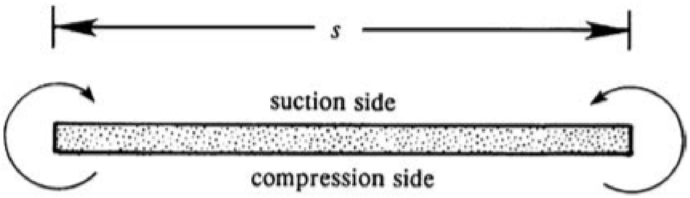

Figure 2-8: Schematic backside view on airfoil with finite span s. [2]

The chord length of the profile at the tip is an important parameter regarding induced drag. This is logical, since the origin of induced drag is fluid being convected over the tip of the wing. The aspect ratio of a rectangular wing, is the non dimensional ratio between the span and the cord length, $AR = \frac{s}{c}$. This means that a very long slender wing has a high aspect ratio, while a short, broad wing has a low aspect ratio. A low AR wing has a broader tip over which more fluid can convect. This leads to a stronger tip vortex, and therefor a larger induced drag. For a wing with a high AR, a lesser strong tip vortex is induced, consequently the induced drag is smaller.

The induced drag is caused by pressure differences on both sides of the wing. Consequently, it is related to the lift distribution along the span of a wing. If an elliptical lift distribution is assumed, the induced drag coefficient can be expressed in the lift coefficient, AR and π, equation 2-4 which is shown by Anderson [24]. This equation also supports the earlier made conclusion that a high AR results in less induced drag and vise versa. For pre-stall conditions, a large part of the total drag on a wing is caused by the induced drag [2]. Therefor it is often beneficial to use high AR wings, although this is not always possible due to constructional reasons. If a wing is mounted on a flat plate, the effective aspect ratio, AR_e, may be used in the equations. This flat plate is also referred to as *symmetry plane*. AR_e is calculated by doubling the span length. Consequently, for a rectangular wing, AR_e is twice AR. This means that the induced drag for a symmetry plane mounted wing, is half the induced drag of the same wing not mounted on a symmetry plane. This is logical, since the symmetry plane wing now only has one tip over which a vortex can be generated.

$$C_{Di} = \frac{C_L^2}{\pi AR} \tag{2-4}$$

Prandtl conducted several wind tunnel experiments to evaluate the aerodynamic properties of a wing at seven different aspect ratios. He related the lift and drag data and came to the insight that the drag between two wings with different aspect ratio at a constant lift, is linked following equation 2-5. Still under the assumption of an elliptical lift distribution. This is also demonstrated by [24] and [25]. For clarity, C_{D1} and C_{D2} are the total drag coefficients of a wing with aspect ratio 1 and 2 respectively.

$$C_{D1} = C_{D2} + \frac{C_L^2}{\pi}\left(\frac{1}{AR_1} - \frac{1}{AR_2}\right) \tag{2-5}$$

For a wing with an infinite AR, no tip vortex and consequently no induced drag can be generated. Similarly this is the situation for flow around a 2D wing, which by definition can not have induced drag, since this involves 3D flow. If this is implemented in equation 2-5, this means that two dimensional, sectional, aerodynamic data can be translated into three dimensional data following equation 2-6 and 2-7 for elliptical lift distributions [25, 24]. This is an important aspect of the Lifting Line (LL) theory of Prandtl. In chapter 3, a method for modelling three dimensional flow using Prandtl's LL theory is explained in detail.

$$C_{D_{3D}} = C_{D_{2D}} + \frac{C_L^2}{\pi AR} \tag{2-6}$$

$$\alpha_{3D} = \alpha_{2D} - \frac{C_L}{\pi AR} \tag{2-7}$$

2-3 Ventifoil suction wing

The Ventifoil WASP system developed by Econowind is a device which is based, and for a large part functions, as a traditional airfoil. The physics on which the aerodynamic forces are generated are just as explained in chapter 2-2. The main difference however, is the fact that the Ventifoil is a suction wing. This means that aside from being a traditional wing, boundary layer suction is applied to a specific region on the wing its surface, in order to delay flow separation. The effect of boundary layer suction is explained with more detail in chapter 2-4-2.

2-3-1 Geometry

The Ventifoil is under continuous development, and is currently fabricated based on standard dimensions. The span is at this moment equal to 10 meters. Preparations are made to extend them with three additional meters. By doing this, it is expected that performance will be enhanced because of two reasons; C_{Di} will be decreased because of an increase in AR and the lift force will be increased because of an increase in planform area A. The Ventifoils are not tapered, so the chord length is constant along the span, $c = 2.137$ [m]. The planform area of the Ventifoil, A, is obtained by taking the product of the span and the chord length. Profile dimensions are shown in figure 2-10 and table 2-1.

$$A = c \cdot s \tag{2-8}$$

$$\lambda_T = \frac{t}{c} \tag{2-9}$$

The thickness ratio, λ_T, of the Ventifoil is defined by the ratio of the thickness, t, over the chord length. The Ventifoil has a constant thickness of $t = 1.300$ [m]. Combined with the chord length this results in a constant thickness ratio. No endplate is mounted on these devices.

Since the Ventifoil is making use of boundary layer suction, there is a perforated region on each side of the device. This suction region stretches over most of its span. The boundary layer suction is driven by a ventilator mounted on the inside of the wings profile. Because the suction is applied on relatively small holes, it is reasoned that the low pressure inside the profile is evenly spread over the suction region. Because this pressure is lower than the pressure in the exterior flow, air is sucked to the interior of the profile. The boundary layer dynamics and separation are very reliant on pressure distribution over the suction side of the wing, which makes the location of the suction region crucial [5]. In figure 2-10, the location of the suction region is indicated with θ and θ_m. The suction region of the Ventifoil is shown in figure 2-9 highlighted in yellow. The permeability of the suction region can be defined by the ratio between the total suction area, which is highlighted yellow, and the combined area of the open holes.

The flap makes that the profile is asymmetric over its chord. The flap length of each Ventifoil is 0.462 meters, and is rotated at an angle of 52.87°. While doing so, the perforated surfaces on the high pressure side is blocked so the suction is only applied on the low pressure side of the wing, where flow separation is likely.

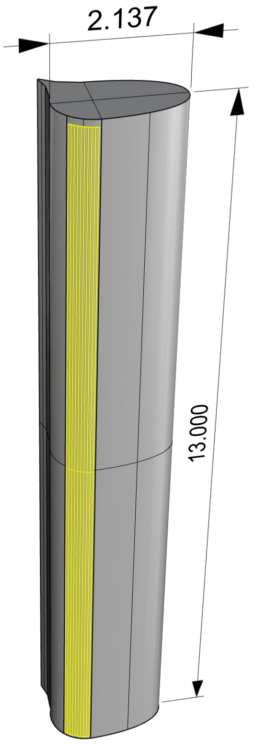

Figure 2-9: Illustration of a Ventifoil.

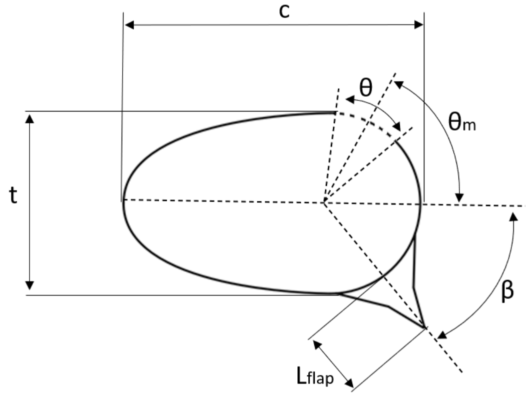

Figure 2-10: Schematic representation of Ventifoil section profile.

Table 2-1: Geometric parameters Ventifoil.

Parameter	Standard	
s	13.000	span [m]
c	2.137	chord [m]
t	1.300	thickness [m]
L_{flap}	0.472	flap length [m]
β_{flap}	52.87°	flap angle
θ	42.1°	suction location
θ_m	66.3°	suction range

2-3-2 Positioning

Ventifoils can be fitted onto ships in different ways. The Ventifoils should not limit the transport capabilities of a vessel, so the most convenient location for installment is mostly governed by the deck layout and structural properties of a certain vessel. This is, on its turn, dependent on the cargo type of the ship. Because of this, there is no standard mounting location for the devices.

One way is mounting the device on a *'flatrack'*. If not in operation, the device can then fold over the deck in transverse direction. This system can be seen in figure 2-2b. The flatrack installation places the devices in longitudinal direction of the ship. By doing so, the distance between each device can be larger than for transverse placement. In some implementation it may enable the installment of more Ventifoils on one ship.

The Ventifoil can also be retrofitted onto a ship. The MV Ankie is an example of two retrofitted Ventifoils. In this configuration the wings are placed on the bow, with seven meters distance between them. This approximately corresponds to a distance of 3.5 times the chord length. This configuration is visualized in figure 2-2a. The distance between multiple wind propulsion devices also has influence on the aerodynamic performance of the system. This will be further explained in chapter 2-8.

2-4 Dominant operational parameters for a Ventifoil

This chapter discusses some important parameters for the aerodynamic properties of a Ventifoil. This is done based on literature and research on the *Turbosail* system of Jacques Cousteau et al. [3]. Cousteau conducted experiments on cylinders with different cross sections, where the thickness ratio was varied between 0.5 and 1. Subsequently the Turbosail obtained a similar profile shape as the Ventifoil. Most data was obtained by experiments. The Turbosail was placed in a wind tunnel with the floor being on one side, and an endplate mounted to the other. His experimental results are shown in figure 2-11a and 2-11b.

2-4-1 Angle of attack

The surface pressure distribution is largely dependent on the shape and angle of attack of the airfoil. The shape of a Ventifoil is characterised as having a large thickness ratio. This results in a moderate curvature at the leading edge and therefor a certain capability of preventing leading edge separation, following the conclusions drawn in chapter 2-2-3. Consequently stall occurs at much higher angles relative to α_{stall} of conventional, slender airfoils.

This is visualized in figure 2-11a. In the left figure, three lift curves are plotted over α. Each corresponds to a different amount of applied suction, which will be explained in the next chapter. For each lift curve, $\alpha_{stall} > 30°$, which is rather high. Consequently, the maximum lift coefficient which can be obtained, C_{Lmax}, is also larger than for conventional airfoils. What can also be seen is that for $\alpha = 0$, the device still produces a considerable amount of lift. This can be attributed to the suction and the flap angle, which makes the device asymmetrical over its chord. However, the difference in $C_{L\alpha=0}$ and C_{Lmax} is still large. This is also endorsed by the pressure distributions at both working points, which are clearly very different. This shown in figure 2-11b.

It is often beneficial to generate high values of C_L. Therefor it is important to configure the device at an angle of attack which is as high as possible, without stalling the Ventifoil. Because in reality the apparent wind angle changes continuously due to short term wind shifts and wind gusts, it is in practice best to choose α to be conservative. The standard setting Econowind applies is a couple of degrees lower than α_{stall}, and is given in chapter 2-7.

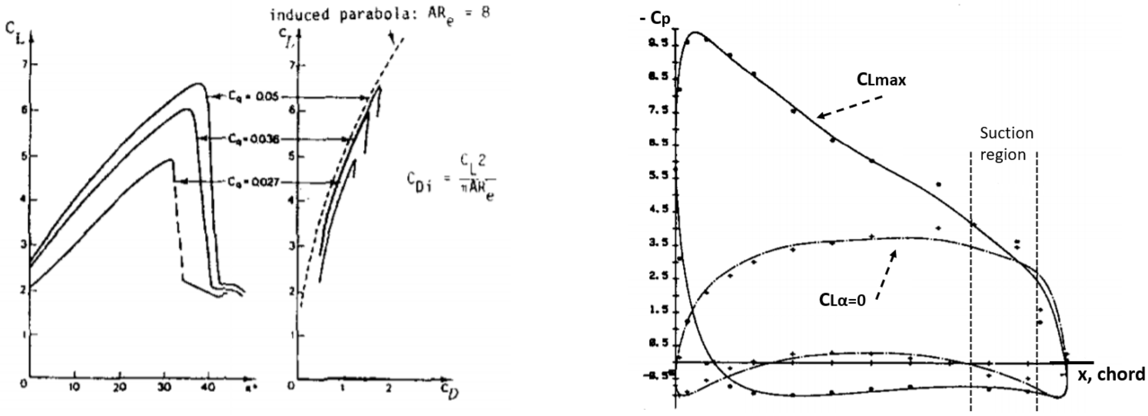

(a) Experimental data of Turbosail.

(b) Pressure distribution over the Turbosail.

Figure 2-11: Turbosail characteristics from wind tunnel experiments. [3]

2-4-2 Boundary layer suction and suction coefficient

The Ventifoil has a high inward curvature at the trailing edge of the profile, as can be seen in figure 2-10. Consequently, the device is prone to trailing edge separation. In order to overcome the adverse pressure gradient, methods are developed to re-energize the boundary layer. One of these methods is applying suction at the trailing edge. This can shift the separation point further downstream. Therefor increasing α_{stall} and C_{Lmax}.

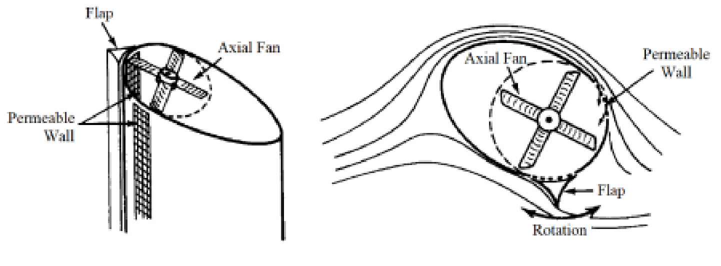

Figure 2-12: Schematic representation of the Turbosail of Cousteau. [4]

Jacques Cousteau was a pioneer in this field and implemented this method in his Turbosail. Through small ventilation holes, located at the trailing edge, the separated air is sucked away from the exterior flow, to the interior domain of the hollow inside of the profile. This way only flow with high kinetic energy, which can overcome the adverse pressure, is left. The boundary layer suction of the Ventifoil is based on the same principles as the boundary layer suction of the Turbosail.

The boundary layer thickness and retardation of flow are very much reliant on the pressure distribution. The amount of applied suction is an important system parameter. The suction coefficient, given in equation 2-10, is a measure for this [26]. Where Q is the mass flux of the air suction, A is the planform area and U is the advection velocity of the incoming flow. The suction power is linearly dependent on the advection velocity. Figure 2-11a shows that the lift and drag is significantly changed by varying C_q.

$$C_q = \frac{Q}{AU} \tag{2-10}$$

The region of suction should be applied directly after the boundary separation point. The separated layer is relatively thin at that location, and the suction is most effective at thin layers. Also the porosity of the ventilated section and shape of the ventilation holes are of importance [26, 5].

In the second graph of figure 2-11a, C_L is plotted over C_D, which gives an important insight. The parabola for the induced drag coefficient, C_{Di}, is plotted. The relation for this curve was given in equation 2-4. What can be seen is that the total drag coefficient almost completely coincides with the induced drag coefficient, which agrees with conclusions drawn in chapter **??**. Hence, it can be concluded that the form drag is negligibly small compared to the induced drag. Therefor, the aspiration seems to be efficient in controlling the boundary layer and reducing the wake.

This seems to be supported by figure 2-11b showing the pressure distribution over the device. For such a blunt object as the Turbosail, a severe adverse pressure gradient is expected towards the trailing edge. However, a steady, mild gradient is observed for C_{Lmax}, which can be ascribed to the low pressure induced by the aspiration. The forces on a Ventifoil are primarily caused by the pressure distribution acting on the Ventifoil surface. In numerical simulations conducted by Lagendijk, only 0.4% of the combined forces was caused by friction [5].

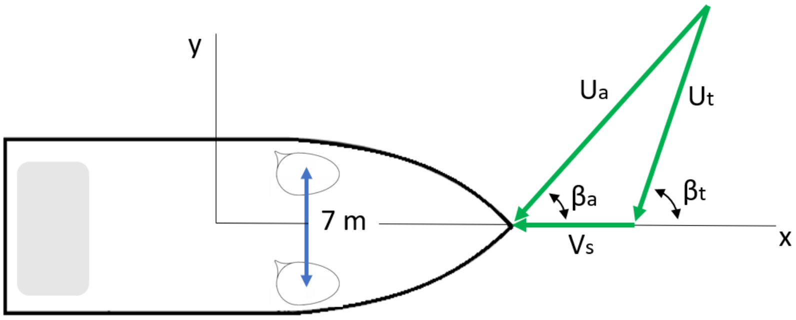

Figure 2-13: Wind vector decomposition on ships axis system.

2-5 Environmental conditions

The forces generated by the Ventifoils are reliant on the wind conditions. The wind characteristics can be expressed in the true wind speed, U_t, and the true wind angle, β_t. Nonetheless, this is not the environment the Ventifoil experiences. The ship also has a forward velocity. This will result in self induced wind vector pointing in the opposite direction of the ships velocity vector and is indicated with V_s. The combination of these two wind vectors will result in the apparent wind velocity, U_a, and the apparent wind angle β_a. These are referred to as the environmental conditions and are the conditions the Ventifoil operate in. A schematic representation of the wind vector decomposition is shown in figure 2-13. Both parameters are calculated using equation 2-11 and 2-12.

$$U_a = \sqrt{(U_t cos(\beta_t) + U_s)^2 + (U_t sin(\beta_t))^2} \tag{2-11}$$

$$\beta_a = arctan\left(\frac{U_t sin(\beta_t)}{U_t cos(\beta_t) + U_s}\right) \tag{2-12}$$

In general headwind is referring to conditions where $0° \leq \beta_a \leq 60°$. Crosswind is referring to conditions where $60° \leq \beta_a \leq 120°$. By downwind conditions often an apparent wind angle of $120° \leq \beta_a \leq 180°$ is meant.

2-5-1 Wind shear

Often the true wind speed and ship speed are used to pre-calculate a uniform wind profile which is then configured as inlet condition in numerical or experimental studies. However, what often is not included, is that true wind profiles (at sea) have a velocity gradient in vertical direction, indicated as the Atmospheric Boundary Layer (ABL). This wind vertical profile is comparable to the boundary layer explained earlier in this chapter. Since $U_t(z)$ is a function of the vertical location, the apparent wind speed and apparent wind angle are also a function of the height, $U_a(z)$, $\beta_a(z)$. The change in $\beta_a(z)$ over the height is called twist and can be very significant depending on the profile of $U_a(z)$. Since the Ventifoil itself has no twist over it's span, this will result in a span-wise varying angle of attack, $\alpha(s)$. Generally,

U_a and α increase over the height of the device. The main objective of this research is to evaluate aerodynamic interaction by means of two methods. In order to perform fundamental analyses, this is further left out of the scope.

Wind gusts and temporary changes in the true wind angle might shortly influence the environmental conditions. Additionally ship movements such as roll influence local instantaneous wind conditions. Nevertheless, for the research goals it is justifiable to neglect these effects.

2-6 Force vector decomposition

Since lift is per definition perpendicular on the incoming flow and drag parallel, the direction of the force vectors is governed by β_a. The magnitude is determined by U_a and system parameters. The lift and drag forces can be transformed using equation 2-13 and 2-14 into a thrust, F_X and side force, F_Y. This thrust force is used as additional propulsion, so that the same ship speed can be maintained while lowering the fuel consumption. A schematic representation of the force vector decomposition is shown in figure 2-15.

$$F_X = F_L cos(\frac{1}{2}\pi - \beta_a) - F_D cos(\beta_a) \tag{2-13}$$

$$F_Y = F_L sin(\frac{1}{2}\pi - \beta_a) + F_D sin(\beta_a) \tag{2-14}$$

The equations clearly show that the thrust will not be large for all environmental conditions, in view of the fact that C_X is dependent on β_a. In the thesis written by Lagendijk [5], a graph for the thrust coefficient over β_a is given for a Ventifoil suction wing at $\alpha = 32°$ and $C_q = 0.04$. This is shown in figure 2-14. It is evident that for crosswinds the WASP device is most effective in generating thrust.

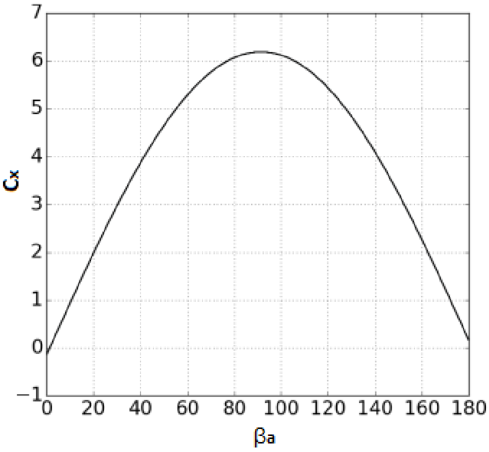

Figure 2-14: C_X over β_a for a Ventifoil. [5]

As is known from paragraph 2-4, each α corresponds to a lift and drag coefficient. From the vector decomposition it can be deduced that the optimum angle of attack varies slightly over

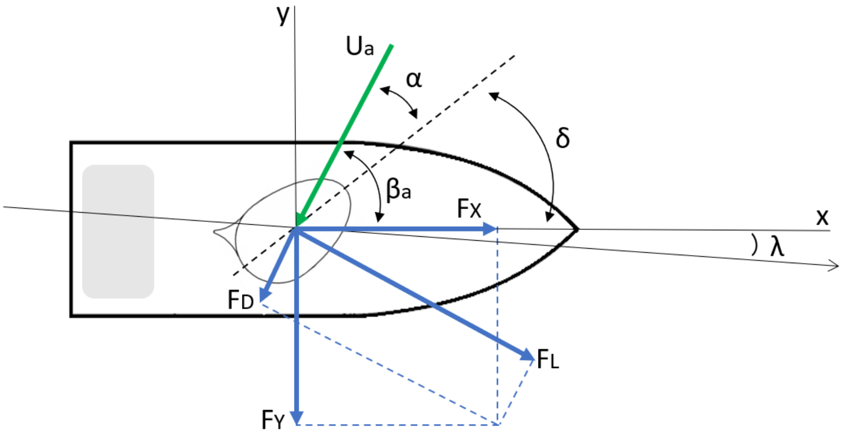

Figure 2-15: Force vector decomposition on ships axis system.

the apparent wind angle. In this sense, the optimum angle of attack is that which generates the largest thrust force.

For headwinds it is important to have an optimal aerodynamic efficiency. This often means that the Ventifoil should not operate at the angle of attack corresponding to C_{Lmax}. Because this also corresponds to a large C_D, and the direction of the C_D vector contributes to a negative thrust force. Consequently, it could be better to operate at a lower α.

For $\beta_a > 90°$, drag also adds to C_X, so it is beneficial to have a large lift force even if this goes together with a larger drag force. The Ventifoil can operate at C_{Lmax} in these conditions.

From approximately $\beta_a > 160°$ it can be more effective to maximize drag because lift is mainly contributing to side force. The Ventifoil can rotate to $\alpha = 90°$, so that C_D will then be the driving contributor to C_X. For that configuration, C_D, and therefor C_X, is mainly dependent on the planform area of the Ventifoil.

The side force, F_Y, will slowly push the ship sideways. Consequently, the ship will sail under a drift angle, λ. This side force will be partly compensated by the hull since it acts as a low aspect ratio lifting body under an inflow angle of λ. However, this results in induced hydrodynamic resistance [27]. The yawing moment induced by the ship generated side force needs to be compensated by the rudder, leading to even more hydrodynamic resistance. If yawing moments on a ship are substantial, this additional ship resistance can have impact on the overall propulsive performance of the ship. These complex physics make it difficult to directly conclude on overall WASP performance in terms of fuel savings, based on only the aerodynamic properties of a WASP device.

The drift angle is assumed small. It's effect on the wind vector decomposition is therefor not included in this study.

A pitch and roll moment are imposed by F_X and F_Y respectively since the point of engagement on the Ventifoil is located above the center of gravity of the ship. Since the longitudinal and transverse stability of commercial ships is often large, it is assumed these effects can be neglected.

Table 2-2: Operational parameters Ventifoil

Parameter	Standard	
α	25°	angle of attack
β_a	[20°, 150°]	apparent wind angles
δ	[−5°, 125°]	sheet angles
U_a	[3.4, 17.1]	wind speeds [m/s]
C_q	0.04	suction coefficient [-]

2-7 Operational envelope

As was reasoned in the previous chapter, not all apparent wind angles are evenly effective for generating a forward thrust. It is evident that at $\beta_a = 0°$, the thrust component of the forces is negative. Also for other low apparent wind angles, C_X can be negative or marginally helping propel the ship.

For very large apparent wind angles, the lift coefficient is mainly contributing to side forces. Therefor the wing can be rotated to a position where $\alpha = 90°$, so that the drag will contribute to C_X. Nevertheless, the planform area of a Ventifoil is relatively small, so the thrust force produced in this configuration is not very substantial.

As is explained in chapter 2-6, there is a theoretical optimal α for each apparent wind angle. Yet, from an operational point of view it is complex to adjust the angle of attack to this theoretical optimum. For this reason the Ventifoil from Econowind operates at a constant $\alpha = 25°$. It is also reasoned that for this setting the Ventifoil only has a significant contribution to thrust for $20° \leq \beta_a \leq 150°$, and operates only in that range of environmental conditions. This means that the sheet angle, δ rotates with β_a over a domain of $-5° \leq \delta \leq 125°$. For apparent wind angles below 20°, the Ventifoils are lowered onto the deck, in order to avoid negative C_X values.

As can be seen in figure 2-11a, the performance is substantially influenced by the suction coefficient at which the device operates. For an increasing C_q, two effects can be differentiated. Firstly, the lift coefficient at $\alpha = 0$ increases, which increases the C_L over the whole range of α. Secondly the stall angle increases, so the range at which the device can operate increases. However, this also comes at a cost. The amount of applied suction is based on the amount of aspiration power, P_a, which is used by the ventilator inside the Ventifoil. Operating at a higher C_q will require more aspiration power than operating at a lower C_q. The Ventifoil is only effective if the power generated from the aerodynamic thrust, is larger than the aspiration power. The power generated from the aerodynamic thrust is equal to the product of F_X and V_s. C_q is linearly dependent on U_a, so the aspiration power will be adjusted on the environmental conditions so that the Ventifoil operates at a standard of $C_q = 0.04$ [-].

The operational domain of the Ventifoil is also limited by structural considerations. The device is made out of light weight aluminium and structurally assessed in order to avoid unnecessary material usage. To avoid structural damage, the Ventifoil operates in apparent wind speeds between 3.4 and 17.1 meters per second. The lower limitation is in order to maintain having larger power savings than power consumption by the ventilator.

2-8 Aerodynamic interaction between wind propulsors

In the application of WASP, it is often usual to install multiple wind propulsion devices. The summation of aerodynamic thrust then makes it possible to even further decrease fuel consumption. This is often also seen in Ventifoil configurations of Econowind. For a combination of wind propulsors, the parameters mentioned in chapter 2-4 are still very relevant. However if multiple devices are mounted in each others surrounding, the behaviour might not be linearly related to that of a single wind propulsor.

In order to get an understanding on this interdependent behaviour, a study on previous research can be done. There are studies which include multiple individual wind propulsors in their setup. The devices might vary between multiple Flettner rotors, soft sails, rigid wings or suction wings. The aerodynamic interaction between these devices is often expressed in terms of differences in C_L, C_D and C_X.

In a fundamental way Garzón shows the influence of having multiple wind propulsors in a flow field. In this study, the flow around four Flettner rotors is visualized using a mathematical model. The results are validated by experimental data. What can be seen is that each Flettner rotor and its individual rotor settings have impact on the total flow field [28].

Also Tillig, Jones et al., and Garenaux et al. perform research on the performance of multiple Flettner rotors. Tillig expresses results in terms of C_X. The latter two compare the lift and drag coefficients of a single, baseline, rotor to the average of a combination of rotors. Both studies obtain the results by means of Computational Fluid Dynamics (CFD) simulations, while Tillig uses potential flow methods. All three studies suggest that the interaction has a significant effect on the aerodynamic characteristics of the devices. Tillig shows that the thrust coefficient of two rotors decrease, while the thrust coefficient of the other two rotors increase, indicating that the relative location of the devices is important [17]. Jones et al., states that for all relative placements, the lift coefficients are lower and the drag coefficients higher. Additionally it is explained that the interaction effects are less severe for a greater distance between the rotors and specific relative positions [15]. Garenaux et al. finds that if three rotors are placed on a ship, the lift and drag coefficients for each rotor is different. However, because the rotors are in this research placed on a hull geometry it is difficult to distinct rotor-rotor interaction from hull-rotor interaction. The researcher state that it is plausible that rotor-rotor interaction effects occur[13]. The consenting conclusions of these three studies are endorsed by the findings of Bordogna. In his dissertation extensive research is presented on the interaction effects of Flettner rotors and rigid sails. Among the conclusions is that the relative location of the devices is crucial and that for a large enough absolute distance the interaction effects disappear [11].

In his report Tillig explains that the interaction can be segregated in potential flow effects and viscous flow effects. Potential flow effects are the bound vortex and tip vortex created by the Flettner rotor. These vortices can be expressed in terms of the circulation created by the rotor and are therefor coherent to the amount of lift the device generates. These potential flow effects have influence on the direction of the flow and on the magnitude of the flow velocity. Viscous interaction is caused by the viscous wake behind a device. In this wake the turbulent kinetic energy can be very large and often a mean velocity reduction applies [17]. Furthermore vortex shedding can be present in the wake, which also leads to a mean velocity reduction. Bordogna agrees with the segregation of potential and viscous flow effects. In his dissertation it is explained that the change in flow direction upstream of a rotor or rigid sail due to potential flow effects generally leads a locally increased angle of attack. The change in flow direction downstream generally leads to a decrease in angle of attack. The first is referred to as upwash, the latter as downwash [11]. Flow direction and velocity are continuous variables in the domain around the device. It is for this reason, that the explanations presented by [17] and [11] are in line with the observations that the aerodynamic properties of a single device, in a set of multiple of devices, are related to the relative location of each independent device.

The studies mentioned above clearly show that interaction effects between wind propulsors influence performance of the total system. Some papers present results where differences between performance of single systems and multiple systems is clearly quantified. By evaluating these results, more in depth knowledge on interaction effects can be obtained.

Fujiwara and Ouchi et al. have conducted research on a cascade of sails and wing sails respectively. Results regarding the performance of the installation are expressed in the difference between a single sail C_X and the average C_X of the plural configuration. Both studies agree that for upwind and downwind conditions the performance is decreased severely by tens of percentages [29, 30]. It is stated by [29] that for cross wind the performance is only slightly lower, while [30] concludes on a comparable C_X for cross winds. This is endorsed by the paper presented by [16]. In this study the results show the C_L reduction rate can amount up to 35% for the total system. Nakashima et al. states that the performance of the most upstream wing is increased, while the performance of the downstream wings are severely decreased, which agrees with the findings of Fujiwara [29, 16]. Research done by Lee et al. shows that the reduction of C_X for a multitude of airfoils compared to a single airfoil is significant and varies between a reduction of 21% and 43% depending on the apparent wind angle. The reduction is again less severe for cross winds, which agrees with [30, 29, 16]. However, in this study no improvement of the upstream device is mentioned.

The studies mentioned above had a fixed positioning of devices and evaluated aerodynamic interaction and change in performance over a range of apparent wind angles. This is also done by Li et al. and Bordogna, but in addition to varying β_a, the absolute distance between the devices is also changed. Li et al. places three wing sails at a distance of 1, 1.5 and 2 chord lengths in a windtunnel, Bordogna uses a distance of 2.5 and 4 times the chord length. The results show that the absolute distance between the devices is an important parameters regarding aerodynamic interaction. For smaller distances, the performance reduction is generally larger. What is remarkable, is that for upwind conditions, a smaller distance actually can lead to better performance. For larger β_a, C_X increases with the absolute distance [31]. Bordogna also shows that interaction effects can contribute to performance [11].

The importance of relative positioning has been clearly demonstrated in the literature. This relative positioning is a function of the absolute distance between the devices, D, and the apparent wind angle β_a. Most studies show a decrease in performance although the severity differs with positioning. It is also shown that it is possible to obtain an increase in performance. Since the behaviour of flow around multiple wind propulsors is complicated, it is interesting to take a closer look at two studies done by Fu et al. and Faure et al.. regarding the effect of relative positioning on the performance of a double airfoil configuration. The most detailed research is done by Fu et al. in which the relative position is given in terms of a distance parallel to the flow direction and a distance transverse to the flow direction.

It is explained that C_l responds to changes in the transverse distance. If the downstream airfoil is placed directly behind the upstream airfoil, C_l decreases due to the velocity deficit of the wake, and the change in flow direction. If this distance is large enough, no interaction is found. The distance in parallel direction is also affecting the aerodynamic properties of the airfoil profiles. If this distance is decreased, the effect of change in flow direction is more pronounced, consequently there is a change in C_l and C_d [32]. The interaction is less severe if the parallel distance is increased. These findings are confirmed by the results presented in [10]. Furthermore the report of Fu et al. defines decalage as the difference in the angle of attack of both airfoils. Based on a Design Of Experiments (DOE) method and regression analyses it is determined that decalage is the most crucial parameter in affecting the aerodynamic performance of the dual airfoil configuration [32]. The downstream airfoil operates in the downwash of the upstream airfoil, consequently, the local angle of attack changes. If α of the downstream wing is increased, the combined C_l increases by anticipating on the downwash effect.

It can be concluded that the location of wind propulsors, relative to each other, and relative to the wind direction, has much influence on the severity of aerodynamic interaction. In more detail, the relative location mostly determines if interaction effects are significant. If interaction is significant, the relative angle of attack between airfoils is a crucial parameter. Knowing this, literature gives interesting insights on the impact of relative angle of attack on the aerodynamic performance of WASP systems.

Wagner conducts an optimization study based on interaction effects for a cascade of six square rigged masts. A configuration based on equal α and a configuration based on a gradually, downstream increasing α are compared. The results show that the graduated arrangement leads to a large increase in lift over drag ratio [33]. This is also shown by other studies. For example Fujiwara increases α for four sails with a couple of degrees for each subsequent sail in downstream direction. The resulting increase in C_X, was averaged over the entire range of apparent wind angles. Compared to a configuration with equal angles of attack, an increase of 7% was observed [29]. Nakashima implements the same strategy on two rigid wings for $\beta_a = 30°$ and $\beta_a = 150°$. A benchmark configuration where both wings are set at $\alpha = 15°$ is compared to a configuration where the downstream wing is set at $\alpha = 20°$. By doing this the total C_L is increased by 23.7% for $\beta_a = 30°$ and for $\beta_a = 150°$ by 22.6% with respect to the benchmark configuration. For the upwind condition, the performance even exceeded the performance of a single sail, indicating that the interactions are beneficial for the system [16]. The paper from Li et al. also attempts to maximize thrust coefficients by independently configuring the angle of attack for $\beta_a = 30°, 60°, 120°$. Increasing the angle of attack for each wing in a cascade of three wings, resulted in an increase of thrust. Compared to a benchmark configuration with equal angles of attack, C_X is increased with 42.3%, 27.7% and 9.3% respectively. However, the aerodynamic performance of the cascade was still less than that of a single sail [31]. Lastly, the study of Lee et al. also present results regarding the optimization of a cascade of three wings. The thrust coefficient is maximized by independently changing the angle of attack and the flap deflection angle for $\beta_a = 45°, 90°, 135°$. Increasing α in downstream direction in order to adjust to the downwash gave the best results. The optimized configuration let to a performance increase of around $10\% - 17\%$. However, the obtained average thrust coefficient is still lower than the thrust coefficient of a single wing. This indicates that only a part of the interaction induced performance losses was recovered by independently configuring the wings [34].

All of the mentioned studies prove that the presence of a wind propulsor in a flow field, is inevitably related to flow field distortion. The potential flow effects in the form of circulation results in a change in flow angle, and a change in flow velocity. Viscous flow effects further disturb the flow field. Flow separating from the body results in a wake field where velocity varies from the far field advection velocity. From there on, it is evident to conclude that a second wind propulsor, placed in the disturbed field, will perform differently compared to being placed in an undisturbed flow field. The effect is mutually, so multiple wind propulsors sharing a flow field, will perform different than a superposition of multiple isolated wind propulsors. The relevance of this aerodynamic interaction is endorsed by multiple studies conducted on different types of wind propulsors. Potential effects such as circulation, and viscous effects such as wake occur at all mentioned wind propulsion devices, including the Ventifoil. Therefor these conclusions are also qualitatively relevant for the Ventifoil WASP system.

The aerodynamic performance of a multitude of devices can be seriously reduced compared to the performance of a single device system. The reductions presented in papers may vary between 10% and 40% mostly depending on the relative placement. The longitudinal and transverse location of wind propulsors on a (imaginary) deck, in combination with the apparent wind angle are therefor important when considering interaction effects. Additionally, the angle of attack of each device is an important parameters, since local conditions will vary because of up- and downwash.

It is possible to adapt to aerodynamic interaction. Multiple studies present results on performance improvements. Improvements are often obtained by increasing the angle of attack of the downstream airfoil and decreasing the angle of attack of the upstream airfoil. Also a strategically positioning of devices may lead to an improved performance. These adaptions may increase the performance by a few percentages up to even tens of percentages. The reduction of performance compared to stand alone devices is usually not, but in some particular cases, completely recovered by the optimizations.

Chapter 3

Methodology

This chapter focuses on the methodology for modelling the Ventifoil using both the lifting line theory and Reynolds Averaged Navier Stokes (RANS). The first paragraph elaborates on various relevant flow phenomena and the corresponding mathematical background. The second paragraph discusses the classical lifting line theory, the modern numerical modelling and implementation on the Ventifoil. Also limitations, a validation and verification study will be presented. Finally the modelling methodology of RANS modelling will be discussed. Multiple topics in this chapter are based on fundamental literature such as *'Fluid mechanics'* by Kundu, Turbulence by Nieuwstadt and *'Ship Resistance and Flow'* by Larsson, [2, 35, 36]. Additionally, personal lecture notes from the course *'Advanced Fluid Dynamics'* are used as source of information [37].

3-1 Vorticity and circulation

Vorticity is a measure for the rotation of fluid particles. It is kinematic vector quantity for fluid flow. It is computed by taking the curl of the velocity field. Vorticity is therefore per definition orientated orthogonal to the velocity vector.

$$\vec{\omega}_i(\vec{x},t) = \vec{\nabla} \times \vec{u}_i(\vec{x},t) \tag{3-1}$$

If $\omega \neq 0$, the flow is *rotational* and the particles are rotating around their own axis. If $\omega = 0$, the fluid is *irrotational* and the fluid particles are not rotating around their own axis.

Circulation is a scalar quantity and a macroscopic measure for the rotation in a flow. It is equal to the line integral along closed contour C of the velocity vector on an infinitesimal small contour element. This is shown in equation 3-2, where $\vec{u}\,\mathrm{d}\vec{l}$ is equal to the velocity component of $\vec{u}$ along the tangential of $\mathrm{d}\vec{l}$.

$$\Gamma = \oint_C \vec{u}\,\mathrm{d}\vec{l} \tag{3-2}$$

3-1-1 Stokes theorem

Stokes theorem delivers the bridge between vorticity and circulation. The theorem reads that the line integral of the velocity field along a closed contour C, is equal to the flux of the curl of the velocity field over surface S made by contour C [2]. Mathematically this is expressed as shown in equation 3-3

$$\iint_S \vec{\nabla} \times \vec{u} \cdot \hat{n} \, \mathrm{d}S = \oint_C \vec{u} \, \mathrm{d}\vec{l} \tag{3-3}$$

By substituting equation 3-1, we can now obtain the circulation by integrating the dot product of the vorticity in that area and the normal vector of S, over area S. It is an expression of the strength of a vortex tube with a cross-sectional surface area S.

$$\Gamma = \iint_S \vec{\omega} \cdot \hat{n} \, \mathrm{d}S \tag{3-4}$$

3-1-2 Irrotational vortex

It is convenient to use cylindrical coordinates to describe the basic principles of vortex dynamics. Imagine an area S with distributed vorticity. If the planar vorticity is then concentrated at exactly $r = 0$ and in the rest of the domain the vorticity is zero, the resulting flow field can be described as being a vortex with strength Γ. Mathematically the following applies:

$$\omega(r = 0) = \infty$$
$$\omega(r > 0) = 0$$

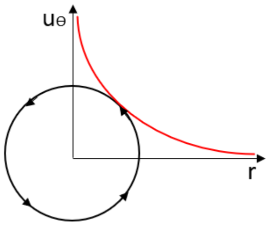

Figure 3-1: Radial velocity of an irrotational vortex.

This results in an infinite vorticity at an orthogonal line on S, at the center of the flow, $r = 0$. Because the flow everywhere else is irrotational, which is a property of potential flow, this is also called an ideal line vortex [2]. More often it is called an irrotational vortex. The velocity field of an irrotational vortex is then defined by:

$$\vec{u} = \begin{bmatrix} u_r \\ u_\theta \\ u_z \end{bmatrix} = \begin{bmatrix} 0 \\ \frac{\Gamma}{2\pi r} \\ 0 \end{bmatrix}$$

This shows that the angular velocity induced by the vortex with strength Γ decreases when further removed from the vortex centerline. If $r \to 0$, the radial velocity goes to infinity. Therefor the centerline of is a singularity regarding the velocity of particles. The irrotationality of the flow can be proven with the use of equation 3-1.

$$\omega_z = \frac{1}{R}\frac{\partial}{\partial r}\left(R\frac{\Gamma}{2\pi R}\right) = 0 \tag{3-5}$$

However the circulation is not zero and is independent on radius r. This can be proven using equation 3-2 and integrating the velocity field over 2π and arbitrary radius R.

$$\Gamma = \int_0^{2\pi} \begin{bmatrix} 0 \\ \frac{\Gamma}{2\pi R} \\ 0 \end{bmatrix} \cdot \begin{bmatrix} 0 \\ R\,\mathrm{d}\theta \\ 0 \end{bmatrix} = \frac{\Gamma}{2\pi} \int_0^{2\pi} \mathrm{d}\theta = \Gamma \tag{3-6}$$

3-1-3 Kelvin's theorem and Helmholtz theorem

Kelvin's theorem states that the circulation around a closed circuit C remains constant in time under the following four assumptions:

- No viscosity or zero net viscous forces over C.
- Body forces on fluid particles are conservative.
- Fluid density is constant or only dependent on pressure.
- The frame of reference is inertial.

This can be proven by time differentiating equation 3-2 and applying the assumptions. Mathematically the result is:

$$\frac{D\Gamma}{Dt} = 0 \tag{3-7}$$

Based on the same assumptions, Helmholtz was able to prove the four following properties of vortex dynamics, which is called the Helmholtz theorem:

- Vortex lines are convected with the fluid.
- The strength of a vortex tube is constant along its length.
- A vortex tube can not end in fluid, it either is; infinite, semi-infinite, a vortex ring or it ends at a boundary.
- The strength of a vortex tube remains constant in time.

3-1-4 Biot-Savart law

An ideal line vortex, only has vorticity in its centerline. However, it does have circulation and the particles in the flow field around the centerline have a radial velocity due to this circulation. When looking at the flow field around a straight and infinite vortex line, the induced velocity in an arbitrary point P, due to circulation Γ, follows from the Biot-Savart law [2].

$$\vec{V_i}(\vec{x_p}) = \frac{\Gamma}{4\pi} \int_{-\infty}^{\infty} \frac{d\vec{l} \times \vec{r}}{|r^3|} \tag{3-8}$$

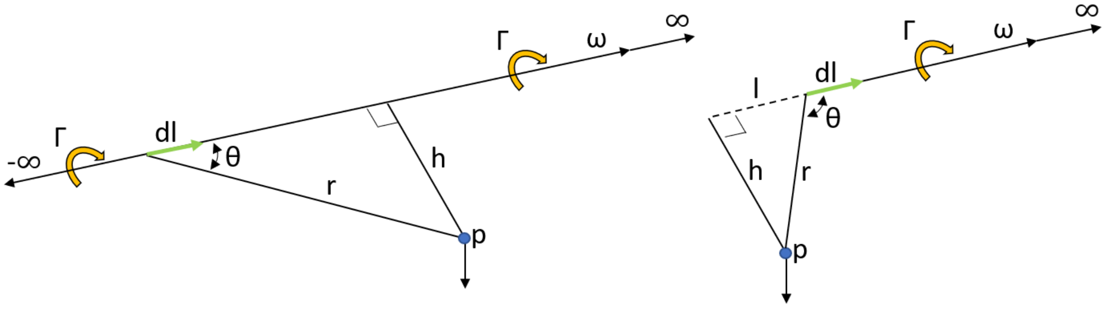

(a) Infinity irrotational vortex.

(b) Semi-infinite irrotational vortex.

Figure 3-2: Straight irrotational vortices.

The magnitude of the induced velocity can be derived using the geometrical relations underneath, derived from figure 3-2a:

$$r = \frac{h}{sin\theta} \qquad l = -\frac{h}{tan\theta} \qquad dl = \frac{h}{sin^2\theta}d\theta$$

$$\vec{V_i}(\vec{x_p}) = \frac{\Gamma}{4\pi}\int_0^{\pi} sin\theta d\theta \tag{3-9}$$

When this function is integrated over the whole length of the infinite line vortex, the resulting induced velocity is similar to the radial velocity component of the flow field of an irrotational vortex. As can be seen, an infinite velocity is induced for $h = 0$.

$$\vec{V_i}(\vec{x_p}) = \frac{\Gamma}{2\pi h}$$

For a semi-infinite irrotational vortex, the boundaries of the integral change with respect to angle between the directional vector $\vec{r}$ and the direction of the semi-infinite line vortex, figure 3-2b.

$$\vec{V_i}(\vec{x_p}) = \frac{\Gamma}{4\pi}\int_\theta^{\pi} sin\theta d\theta \tag{3-10}$$

3-2 Lifting line theory

This paragraph will elaborate on the lifting line theory and how this theory can be used for modelling lifting devices.

3-2-1 Kutta-Joukowski lift theorem

If a two dimensional airfoil is placed in ideal flow, no lift will be generated. One stagnation point will be located on the suction side of the airfoil and the other on the pressure side of the airfoil. However, there is a theory developed as a method for including viscous flow effects to the assumed non viscid ideal flow. This is called the Kutta condition. The Kutta condition holds that after leaving the trailing edge, it continues in the direction of the trailing edge, as if the trailing edge of the airfoil was extended a bit further [38]. In order to accomplish this, circulation is needed. By adding this circulation to the steady ideal flow, the stagnation point on the suction side is moved to the sharp trailing edge of an airfoil. The process is illustrated in figure 3-3. In the first scenario the wing is given an instantaneous velocity U in a stationary fluid domain. The rear stagnation point is located at B on the suction side and the flow velocities and vorticity around the trailing edge are singular. In the second scenario, the boundary layer on the pressure side is developed and separates the flow from the trailing edge. The vorticity generated by this shifts the rear separation point to the trailing edge, as is shown in scenario 3. The Kutta condition is now satisfied.

The vorticity which was needed to create the steady flow of the Kutta condition advects with the fluid flow and is called the *starting vortex* [2]. If a closed circuit ABD is drawn around and moving with an airfoil and a closed circuit BCD is drawn around the starting vortex, we can prove the existence of a bound vortex around the airfoil. This is illustrated in figure 3-4.

Based on Kelvin's and Helmholtz theorem, it is known that for an incompressible, ideal fluid, with conservative body forces, irrotational flow will always remain irrotational in a closed circuit. Since the Kutta condition was applied on an initially stationary flow, the total vorticity and therefor circulation in the total domain $ABCD$ should stay constant in time $\frac{D\Gamma}{Dt} = 0$. After the development of the Kutta condition, the total circulation in BCD is Γ_{Kutta}. This means that there should exist a vortex of equal strength Γ and counter rotating to Γ_{kutta} in the circuit ABD.

This vortex is called the bound vortex, since it is moving with the airfoil. The Kutta-Joukowski lift theorem relates the strength of the bound vortex to the lift force produced by a two dimensional airfoil in steady ideal flow [2].

$$F_l = \rho U \Gamma \tag{3-11}$$

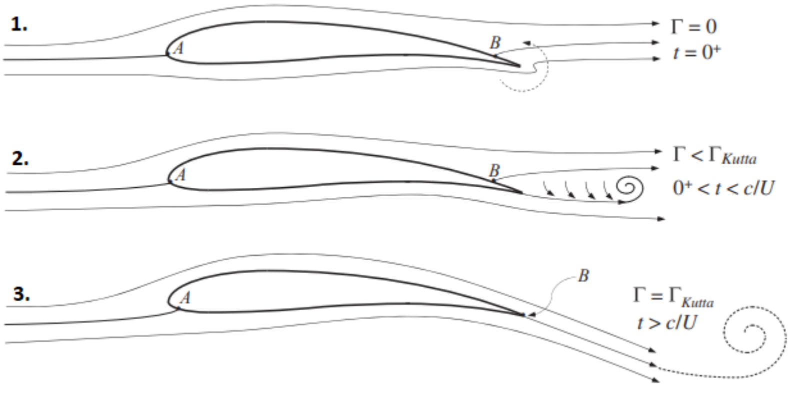

Figure 3-3: Development of Kutta condition over time t. [2]

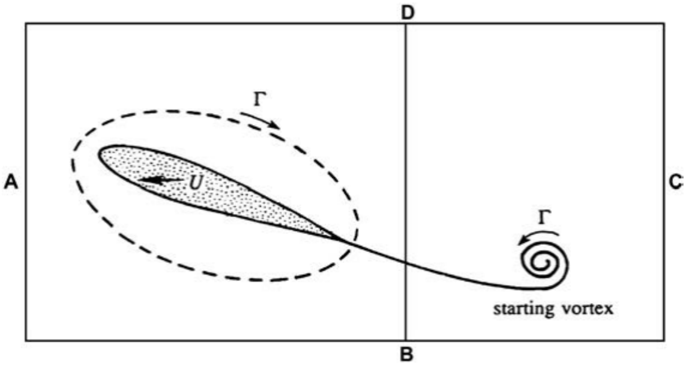

Figure 3-4: The bound vortex and starting vortex in a closed fluid domain. [2]

3-2-2 Three dimensional vortex systems

As explained in paragraph 2-2-4, flow around a three dimensional wing will induce vortices which are convected downstream. It was explained that the vorticity will roll up and concentrate into tip vortices. As is described by Helmholtz theorem, a vortex tube can not end in a fluid. This hypothesis is then full filled because the tip vortices are actually an extension of the bound vortex. The end of the tip vortices are on its turn connected to the starting vortex explained in paragraph 3-2-1. A visualization is given in figure 3-5b. However, since the starting vortex assumed to be very far removed from the wings vortex system, its influence on the flow can be considered insignificant. The tip vortices then become semi-infinite vortices. Consequently, the theory of Helmholtz still holds as the circulation is still conserved in the domain.

$$\Gamma_{bound} = \Gamma_{tip1} = -\Gamma_{tip2} = -\Gamma_{starting} \tag{3-12}$$

As will be later explained, the the interaction between vortices will be left out of consideration when modelling the vortices in a three dimensional system as ideal line vortices. Then, the vortices do not roll up into two tip vortices, but continue in the domain from the location where bound vorticity is shed. This leads to what is called a vortex sheet, illustrated in figure 3-5a. This vortex sheet exists of multiple horse shoe vortices. Circulation is still conserved in the domain.

3-2-3 Classical Lifting line theory - mathematical modelling

The classical Lifting Line (LL) theory of Prandtl is based on the vortex system schematically showed in figure 3-5a. The most important aspect, and also the origin of the theory's name, is that the physical geometry of the airfoil is replaced with an ideal line vortex, the bound vortex. This is the lifting line and is often originated at a quarter of the chord length of the wing. The bound vortex has a continuous distribution of strength $\Gamma_{bound}(s)$.

Secondly, the flow over each wing segment in span-wise direction is assumed to be two dimensional and that C_l is linearly dependent on the angle of attack on that segment. For that first to hold, the wing should have a large aspect ratio. The latter is satisfied for small angles

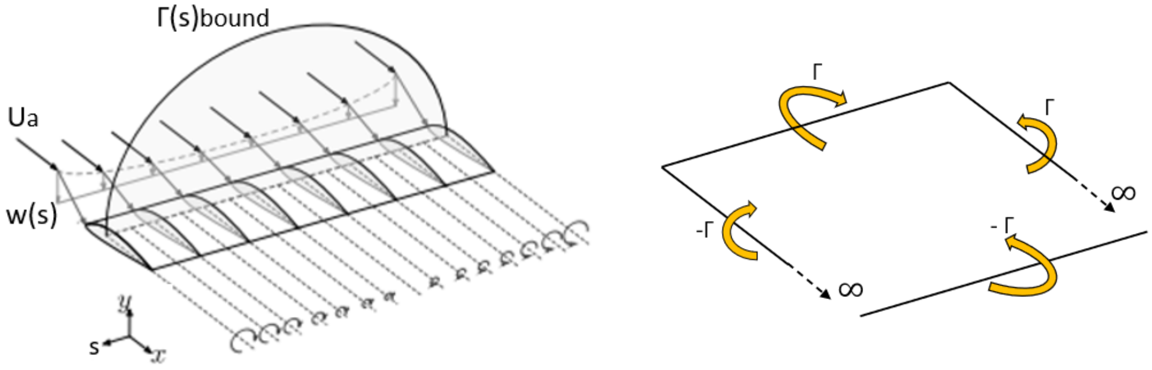

(a) Bound vortex and trailing vortex sheet. [39]

(b) Horse shoe vortex.

Figure 3-5: Schematic representation of discretized vortex systems.

of attack.
Thirdly, the classical lifting line theory ignores interaction between vortices in the trailing vortex sheet [2]. Therefor, the trailing vortex sheet is not rolled up into two tip vortices and remains a sheet as shown in figure 3-5a. Based on these assumptions Prandtl's LL theory gives an analytical expression for span-wise lift distribution of a three dimensional wing.

It starts by finding an expression for the influence of the velocities induced by the trailing vortices, on the bound vortex. Because of the orientation of the circulation, the induced velocities are orthogonal to the wing. This is called downwash. The downwash in front of the lifting line is less severe than the downwash behind the lifting line, as this location is located further away from the semi-infinite vortex sheet.

As is known, the induced velocity is singular on the centerline of an irrotational vortex. This difficulty is omitted by defining that the self induced velocity on the centerline at zero. Consequently, the bound vortex does not induce velocities on itself. This is all derived from the Biot-Savart law as discussed in chapter 3-1-4. The downwash from the trailing vortex sheet on an arbitrary point s_1 on the lifting line, is calculated using:

$$w(s_1) = \frac{1}{4\pi} \int_{-\frac{s}{2}}^{\frac{s}{2}} \frac{d\Gamma}{ds} \frac{1}{(s_1 - s)} ds \tag{3-13}$$

As the resulting downwash distribution, $w(s)$, is directed orthogonal to the wing and incoming flow, and combined with the undisturbed flow vector U_a, the effective flow vector is altered by means of direction and magnitude, resulting in U_{loc}, illustrated in figure 3-6. The change in flow angle is called the induced angle of attack, α_i. The induced angle of attack can be approximated by equation 3-14, since often the downwash is considered small relative to the undisturbed flow velocity. The effective angle of attack, α_e, is then the difference between the undisturbed angle of attack, α_∞, and the induced angle of attack, shown in equation 3-15. The lift vector, which is defined as orthogonal to the flow direction, can then be defined based on the direction of U_{loc}. This leads a lift vector which is rotated by α_i indicated as dL_e in figure 3-6. The component of this new vector which is directed parallel to the undisturbed flow U_a, is the induced drag, shown as dD_i.

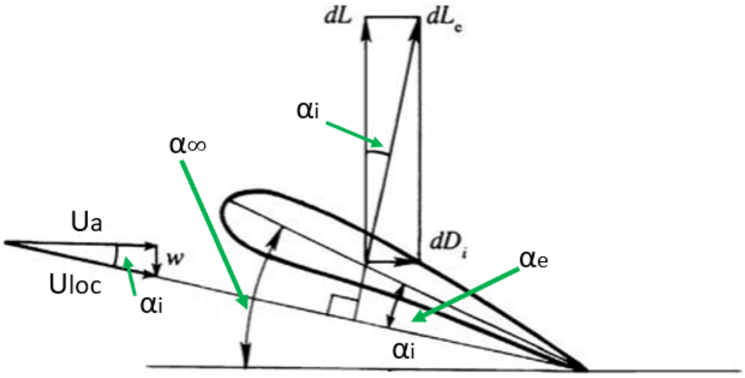

Figure 3-6: Force vectors and α_e, due to downwash on an airfoil section.

$$\alpha_i \approx \frac{w}{U_a} \tag{3-14}$$

$$\alpha_e = \alpha_\infty - \alpha_i \tag{3-15}$$

Derived from the Kutta-Joukowski lift theorem, equation 3-11, two dimensional lift coefficient on a section can be expressed as:

$$C_l = \frac{\Gamma}{\frac{1}{2}U_a c} \tag{3-16}$$

Again, the sectional lift coefficient is linearly dependent on the angle of attack, so with the inclusion of downwash of the trailing vortex sheet, the 'new' two dimensional lift coefficient can be computed. This is done via equation 3-17. Where the derivative of C_l over α is the slope of the two dimensional lift curve.

$$C_l = \frac{dC_l}{d\alpha}(\alpha_e - \alpha_{C_l=0}) \tag{3-17}$$

By combining equation 3-13, 3-16 and 3-17, an expression for the bound vortex strength under influence of the trailing vortices can be found.

$$\Gamma(s) = \frac{1}{2}U_a c \frac{dC_l}{d\alpha}(\alpha_e - \alpha_{C_l=0}) \tag{3-18}$$

A solution for integral equation 3-19 is often found with the use of Fourier series [39]. Ultimately, the total lift production of the 3D wing is then computed by integrating the strength of the three dimensional bound vortex over the span of the wing.

$$F_L = \rho U_a \int_{-\frac{s}{2}}^{\frac{s}{2}} \Gamma(s)\mathrm{d}s \tag{3-19}$$

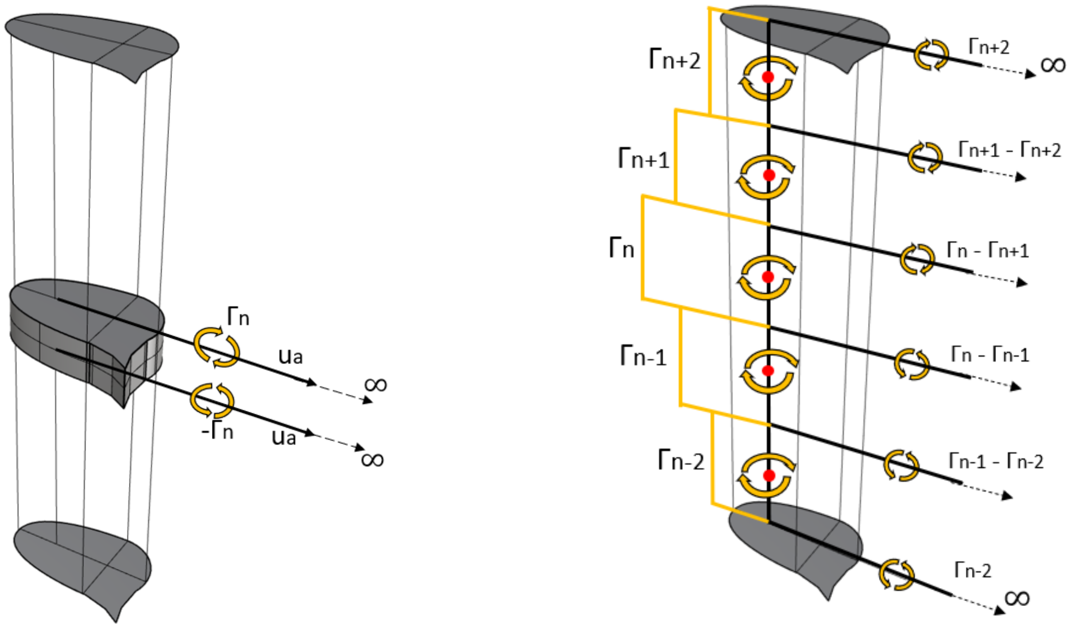

(a) Semi-infinite trailing vortex lines.

(b) Horse shoe vortex systems.

Figure 3-7: Schematic representation of discretized vortex systems.

3-2-4 Modern implementation - numerical modelling

As described above, the classical formulation of the LL theory is based on multiple assumptions. Consequently, this limits the applicability of the theory to certain cases. In the theory described above, the bound vortex does not have a contribution of induced velocities, since the control points are positioned on the centerline of the bound vortex, the lifting line, itself. The assumption that the bound vortex is a straight vortex line is reasonable for straight wings. If a wing has sweep and dihedral, the bound vortex would induce velocities on other positions at the lifting line. The same would go for multiple lifting devices sharing the same flow field [40].

A second limitation is that the assumption that the two dimensional lift coefficient is a linear function of the angle of attack. It is clearly shown in figure 2-7a and 2-11a that this does not hold for near stall, stall and post stall configurations [40, 2, 39]. Because of both limitations, the classical theory is not suited to compute interaction between wind propulsors and higher angles of attack

A numerical method based on the classical theory is proposed by Phillips and Snyder [40], and is capable of solving these two limitations. In this method a lifting surface is discretized into sections. Each section has its own bound vortex and two trailing vortices. This system of three vortices is called a *horse shoe* vortex. The bound vortex lines are located at the a quarter length of the chord line of a discrete wing section. At the end points of the bound vortex, nodal points are located. The trailing vortices start at these nodal points and are aligned in direction of the undisturbed flow [40]. Each discretized section has one control point located at the bound vortex line.

By discretizing the vortex system in such a way, bound vortex lines which are not aligned can now induce velocities on each others control points. The trailing vortices of neighbouring horseshoe vortices are located at the same nodal points. The difference between the bound part of the neighbouring horse shoe vortices is the net vorticity which is shed of the wing section, and therefor also the vorticity of the trailing vortex.

Instead of the integral equation 3-13, the induced velocities in point j on any bound vortex, can now be described by a summation of the influence of N horseshoe vortices. Where Γ_i is the strength and $\vec{v_{ij}}$ is the influence of the vortex corresponding to segment N [40].

$$\vec{V_j} = U_a + \sum_{i=1}^{N} \frac{\Gamma_i \vec{v_{ij}}}{c_i} \tag{3-20}$$

The initial vortex strength of each horseshoe vortex is not known. This is, similarly to the classical theory, approximated by combining the Kutta-Joukowski lift theorem, equation 3-21, with a relation between sectional lift and angle of attack. Nonetheless, this relation does not have to be assumed to be linear this time. It is based on a two dimensional lift curve which should be given as input for the model. Consequently it is explained that this method is capable of capturing near stall behaviour [40].

$$\mathrm{d}F = \rho \Gamma \vec{V_j} \times \mathrm{d}s \tag{3-21}$$

By putting up a discrete system of N horse shoe vortices, the induced velocities can now be calculated over any arbitrary point in the domain. This means that one can place multiple lifting surfaces in a single flow domain and compute the induced velocities on both lifting lines. These induced velocities can be used to compute the effective angles of attack on the control points of each lifting segment and compute lift forces on each segment. By numerical evaluation the lift and drag coefficients for the total wing can then be obtained.

3-2-5 Implementation on Ventifoil

As stated, MARIN is developing a tool which utilizes the method proposed by Phillips and Snyder. This will be used for the evaluation of aerodynamic performance of two Ventifoils at multiple distances.

As discussed in the previous paragraph, the method uses two dimensional lift and drag data is input for its calculations. This first needs to be obtained for the current Ventifoil geometry at the operational parameters explained in chapter 2-7. This will be done by means of RANS simulations as will be explained in chapter 3-4. The geometry will be placed under different angles of attack in order to obtain the two dimensional lift and drag data for $Cq = 0.04$.

Next, a three dimensional Ventifoil with a span of 13 meters will be placed in the flow domain as a lifting surface at the undisturbed angle of attack, $\alpha_\infty = 25°$. A symmetry bottom condition, as is explained in paragraph 2-2-4, is applied. The discretization is done based on an input value which indicates the number of N segments. Furthermore input values are the two dimensional lift and drag data, the free stream vector and the position of the device.

The initial bound vortex strength on each control point, Γ_i, is guessed based on the relation between C_l and α. From the discreet distribution of bound vorticity, the strength of the

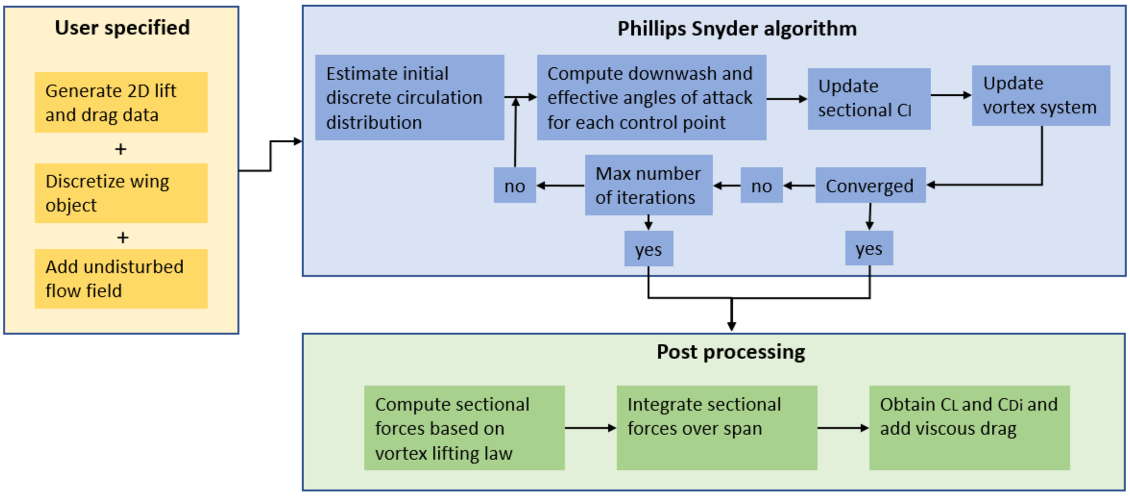

Figure 3-8: Workflow of MARIN numerical lifting line algorithm.

trailing vortices is determined. A matrix containing the strengths and positional parameters of the initial horse shoe vortex system is set up.

From there the induced velocity on each control point is determined using equation 3-20. The induced velocity vector, downwash, and the undisturbed velocity vector are combined in order to determine the induced angle of attack and effective angle of attack, equation 3-6.

Based on the effective angle of attack and the two dimensional lift and drag curve, an estimation for the sectional lift on each segment is done. In this step, it is thus assumed that the flow over the segment is two dimensional.

From the newly computed sectional lift and the vortex lifting law, equation 3-21, an updated bound vorticity can be computed around each control point. From the updated discrete bound vorticity distribution, the strength of the trailing vortices can be found. This way, the vortex matrix is updated for one iteration. The next step is to again compute the induced velocities from the updated vortex matrix. This iterative step is required to find solutions also for the non-linear domain of the lift slope.

This process is iterated until the solution for the bound vorticity converges to a user specified criterion. A relaxation factor may be used to avoid instability. If the solution for the bound vorticity is converged the discrete circulations can be used to compute sectional lift and drag data. The sectional C_l and C_d can then be numerically integrated over the span to obtain C_L and C_{Di}. Because of earlier stated limitations, the computed drag only embodies the induced drag. To retrieve the total drag coefficient, the viscous drag can be added to C_{Di}. This can for example be obtained by doing a single 3D simulation at an angle of attack at which no lift is generated. The viscous drag can also be added per section by using the sectional drag coefficients. The iterative process is illustrated in figure 3-8. For evaluating interaction effects between Ventifoils, two lifting surfaces will be added to the undisturbed flow field. The relative positioning of the objects can be varied. The vortex systems of both Ventifoils will be placed in one vortex matrix. The numerical process is solved similarly as described above, although more iterations may be needed for approaching the convergence criterion.

The process described above and illustrated in figure 3-8, show the iterative process of obtaining three dimensional lift and drag data based on two dimensional input. If the interaction between two Ventifoils degrades the aerodynamic performance, this will be indicated by the resulting C_L and C_D. Moreover, the span-wise discrete distribution of vorticity, induced velocities and induced angles of attack can be evaluated for each Ventifoil. This may give fundamental insights regarding the interaction.

3-2-6 Limitations and assumptions

Although the method proposed by Phillips and Snyder makes way to evaluate multiple lifting surfaces or lifting surfaces with non-conventional shapes, it is still based on some principles and assumptions of Kelvin and Helmholtz theorems. This means that models based on this method still have limitations.

Firstly the vortex lifting laws used are based on steady ideal flow. This means that time dependent flow characteristics are not incorporated in results computed by the method. Also ideal fluid has no viscosity. Consequently viscous effects such as boundary layer dynamics, turbulence and viscous wake fields behind the lifting surface are not incorporated in the model. Viscous lift and drag, such as skin friction, is only partially included in the model via the sectional lift and drag curves.

Secondly, the method still assumes that the aerodynamic behaviour of each segments is similar to the behaviour of a two dimensional segment. This means that the method will not deliver accurate results for very low aspect ratio lifting surfaces.

Thirdly, because of the lack of viscosity, the horse shoe vortices are modelled as being irrotational vortices. Consequently, induced velocities near the center of a vortex line are approaching infinite values, as explained in chapter 3-1-4. This may lead to singularities if control points are closing in on trailing vortex lines originating from another lifting surface.

Finally, especially of importance for suction wings like the Ventifoil, the interaction between pressure fields around the lifting surfaces is not modelled. The suction coefficient of the Ventifoil is likely to be influenced by the gradients in the combined pressure fields.

3-2-7 Modelling errors

When a physical system such as a wing is captured in a model, approximations need to be made. The process from turning physical phenomena into numerical models is divided into different stages. Firstly, the real, physical system needs to be transformed to a conceptual model. In this step, the physical aspects of the model are assessed and evaluated on significance. If an effect is assumed to be less significant, it can be decided to omit this in the conceptual model. For airfoils described by LL theory, this is for example the absence of viscous effects. Next, the conceptual model is described by a mathematical model. The difference between solutions of a mathematical model and reality is called the *modelling error*.

Often the physical concepts are described by integral and differential equations. The expression of downwash due to vortex strength over the span is an example of this, equation 3-13. These continues equations have to be discretized in order to solve them. This is exactly what was explained in chapter 3-2-3 and 3-2-4. The difference between continues results and the solutions to the discrete mathematical model are called *discretization errors*. In the LL method the discretization is done by dividing the span of the wing into small wing segments. The refinement of the discretization and the type of numerical scheme often have a large influence on the discretization error. For a finer discretization and higher order method, the discretization error becomes smaller [36].

The discrete mathematical model is solved through an iterative process. The solution then converges to a solution. The solution is accepted when the difference between two subsequent iterations has become smaller than a user specified convergence criterion. The difference between the accepted solution and the actual solution is called the *convergence error*. Finally an error is made since the computer which solves the solution, rounds the values to a certain amount of decimals. This is called the *round off error*. The discretization error, convergence error and round off error are together the *numerical error* of the model. There are additional types of errors which will be left out of consideration now [36].

Often the convergence and round off errors can be assumed small. Consequently, the numerical errors are dominated by discretization errors. In order to say something about the quality of the model, the discretization error should be evaluated. This is process is called verification. A grid refinement study can be conducted, where the results of each refinement is compared [36].

The refinement of the discretization can be expressed in the distance between to subsequent discretization points. This refinement can be expressed in an independent distance $h = \frac{1}{N}$. Where N is the number of wing segments. If $h \to 0$, the solution of the discrete model should approach the solution of the continues model. This is called the *grid independent solution*. For a third order numerical method, the discretization error reduces with h^3. The difference between the grid independent solution and a solution with an arbitrary discretization spacing h is the discretization error. For RANS simulations, it can be costly to perform simulations for many different grid refinements. A common method for obtaining the grid independent solution is by performing a Richardson Extrapolation on a smaller number of simulations on different grid refinements [41]. For this extrapolation, the order of the numerical scheme has to be known. This is however not clear at this stage.

Fortunately, the computational time for obtaining the aerodynamic coefficients for one configuration using the algorithm developed by Maritime Research Institute Netherlands (MARIN) costs is often less then a second. Therefor a solution can be found for more and finer discretizations. An extrapolation on the results will be done, and the best fit will define the order of the numerical scheme. A Ventifoil with $s = 13$ [m] and $\alpha = 25°$ will be used. The Ventifoil can be discretized by either using a uniform or cosine spaced discretization, shown in figure 3-9.

What can be seen in figure 3-10, is that for a uniform spacing a large amount of N segments is needed in order for the solution to converge to a value of C_L. A third order polynomial can be fitted through the data points, with an R value of 1. It therefor seems that the numerical scheme is of the third order. Extrapolating for $h = 0$ gives $C_L = 5.63024$.

However, for finer discretizations, the computational time also increases. It is known that the span-wise velocity component increases towards the tip of the wing. Also the gradient in the vorticity distribution is larger towards the tip. Therefor it can be reasoned that it is more important to use a finer discretization at the tips than at the midsection. Therefor a cosine spacing is applied for the distribution of segments. This leads to a far better convergence,

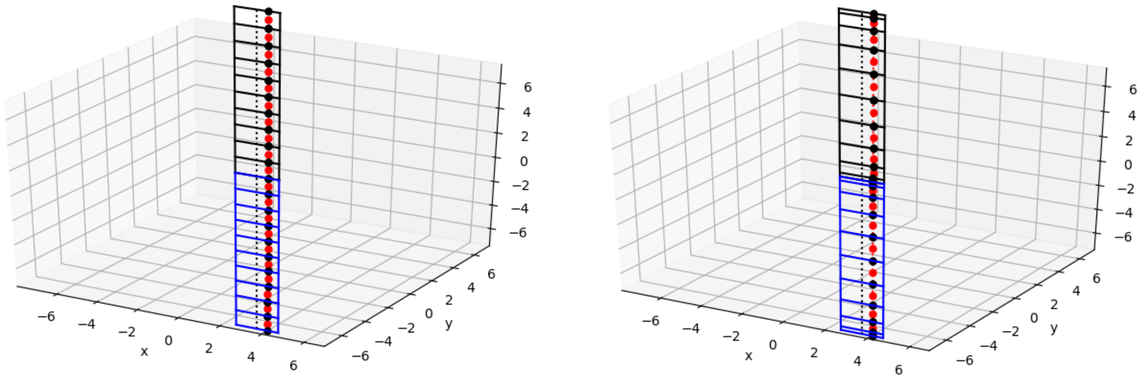

(a) A uniform spacing. **(b)** A cosine spacing.

Figure 3-9: Two discretization methods $N = 10$ with mirror condition.

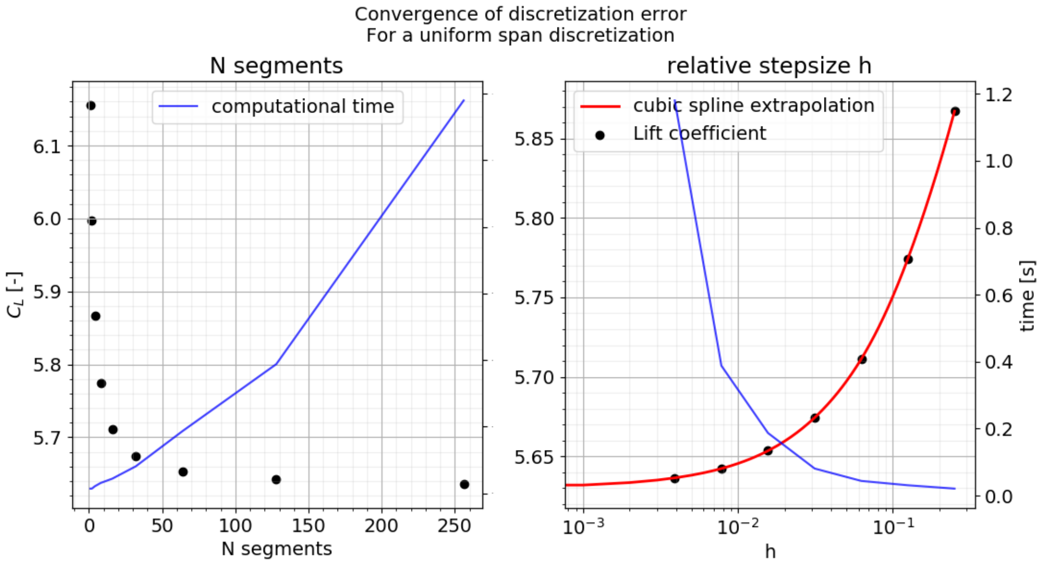

Figure 3-10: C_L for different uniform spaced span discretizations.

shown in figure 3-11. Again a third order polynomial is fitted on the data. Extrapolation for $h = 0$ gives $C_L = 5.63019$, which differs only a fraction form the uniform discretization.

Now that the grid independent solution is known, the discretization error can be computed. What can be seen is that the error for a cosine spacing is much smaller for values of h compared to the uniform spacing. If an discretization error of 0.1% is accepted, this can be reached with $N_{cosine} = 10$. With a uniform spacing this would require $N_{uniform} = 271$. If we than again take a look at figure 3-10 and 3-11 we can see that using a cosine spacing one evaluation would take well below $t < 0.04$ [s]. One evaluation with the same discretization error and a uniform spacing would take $t > 1.2$ [s]. When taking into account that this method would be used to evaluate hundreds of different configurations, due to the large design space, it is evident that the cosine discretization is by far the superior method.

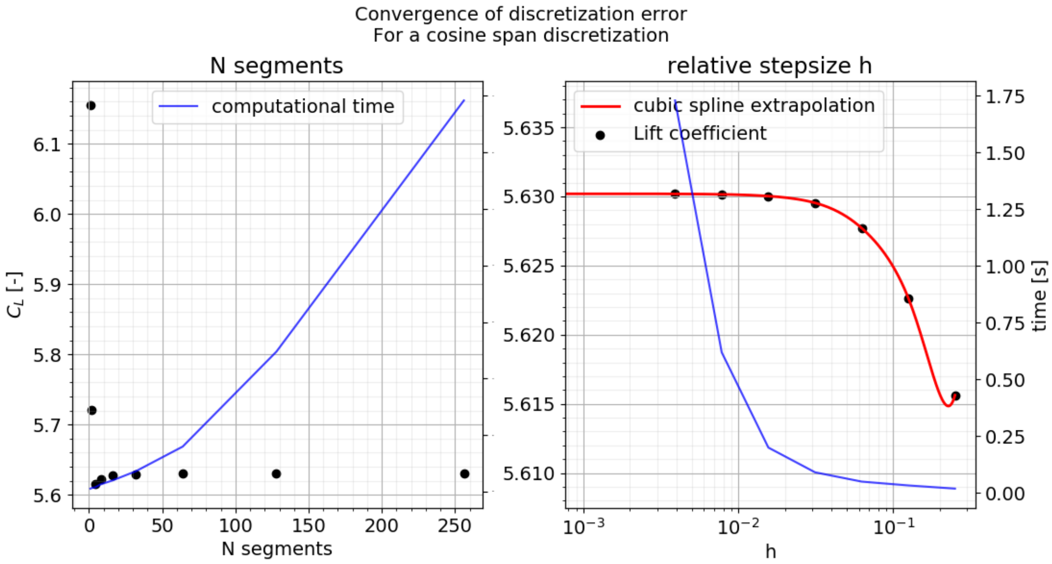

Figure 3-11: C_L for different cosine spaced span discretizations.

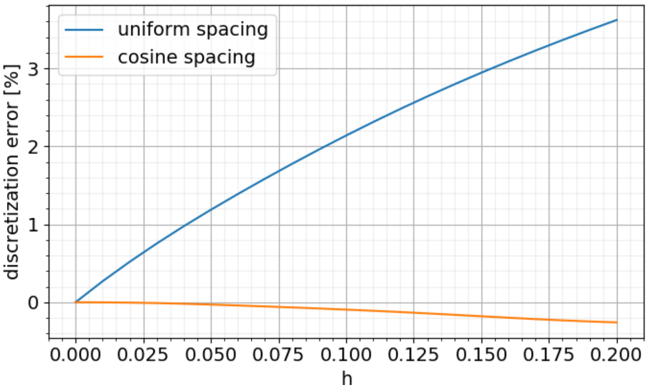

Figure 3-12: Discretization error in percentages for uniform and cosine spacing.

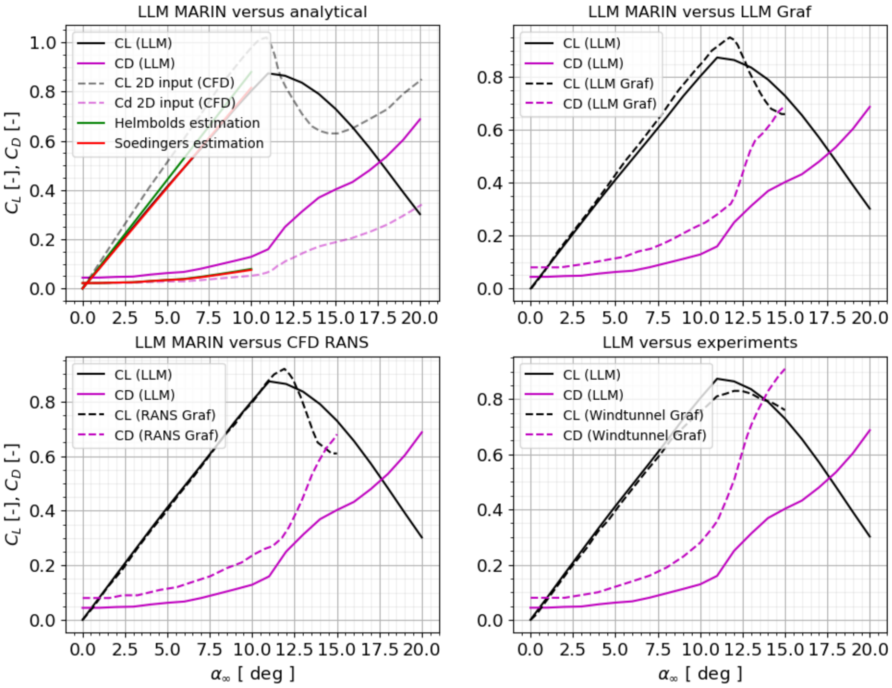

Figure 3-13: Results of MARIN LLM and Graf for a NACA0012 airfoil with $AR_e = 9$. [6]

3-3 Validation of Lifting Line Model

Validation is a process of evaluating the modelling errors resulting from capturing a physical process in a conceptual model [36]. This can be done by comparing results from the Lifting Line Model (LLM) to results from higher fidelity methods, such as Computational Fluid Dynamics (CFD) simulations or experimental results.

A study on aerodynamic performance of a NACA-0012 airfoil is conducted by Graf et al. by means of multiple methods. First, sectional lift and drag data is obtained using RANS simulations. This data is used as input for a lifting line model, obtaining the 3D aerodynamic coefficients. This is then compared to higher fidelity 3D RANS simulations and wind tunnel experiments. The wing used has a span of 1.8 meters and a chord length of 0.4 meter and is placed on a flat plate acting as symmetry bottom condition.

A rigid wing with the same dimensions and symmetry bottom condition is added in the LLM and compared to the results presented in the paper by Graf et al. [6]. Additionally, two analytical expressions for lift and drag are included, being the estimations for C_L and C_{Di} by Helmbolds and Söding [8, 42]. The total drag coefficient is computed by adding C_{Di} to the parasitic drag. The latter is similar to the sectional drag coefficient. The results are shown in figure 3-13.

What can be concluded is that the analytical estimations in the top left figure show good agreement with C_L. The estimation only give a value for the slope of the lift curve. Therefore the values diverge reaching, and only give an approximation, up to α_{stall}. The dashed lines

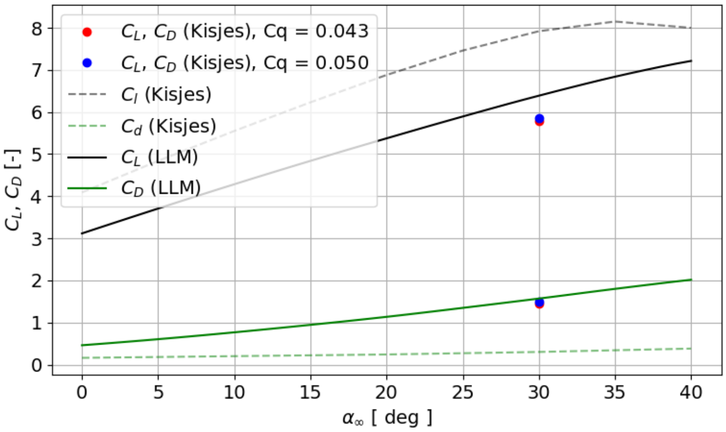

Figure 3-14: LLM of MARIN validated against 3D RANS simulations at $C_q = 0.047$. [7]

indicate the sectional input data. In the top right figure both lifting line solutions are shown. Again good comparison is seen for the lift coefficient. This also applies to the comparison between the LLM and RANS and the wind tunnel experiments. The onset of stall is also satisfactory computed by the LLM. The values for C_D computed by the LLM show rather large discrepancies when compared to the other methods and are underestimated. This is also observed when comparing C_D obtained by both lifting line models. This is remarkable since a similar modelling strategy was used to include drag.

In research conducted by Kisjes, the aerodynamic properties of a Ventifoil with $s = 5$ and $c = 1$ meter were evaluated. Mostly two dimensional CFD simulations were conducted, but for two different suction coefficients three dimensional simulations were done. The 2D results from Kisjes are used as input data to validate the LLM with these two solutions. The results are shown in figure 3-14. An important side note is that the 2D input data was only available for $C_q = 0.047$, while the 3D data was only available for $C_q = 0.043$ and $C_q = 0.05$ [7].

The difference between the 2D input and LLM output clearly show the effect of the difference between α_∞ and α_e. The slope of the lift curve decreased and α_{stall} shifted to higher angles. The 3D data points for $C_q = 0.043$ and $C_q = 0.05$ are very close to each other for both lift and drag. Since the LLM uses input data for $C_q = 0.047$, the curve should lay between the two data points. However, an overestimation for lift and drag can be seen. The overestimation of drag can be a results from the overestimation of lift. Because for higher C_L, the induced drag will also be higher.

3-4 Reynolds Averaged Navier-Stokes modelling

As explained in the research introduction, additionally to the LLM, a higher fidelity method will be used to evaluate aerodynamic interaction. The proposed CFD method will be based on the RANS equations. This paragraph will discuss the conceptual and numerical modelling of the flow via this method. RANS simulations will be conducted for a two dimensional Ventifoil section, a three dimensional single Ventifoil and configurations existing of a pair of three dimensional Ventifoils.

3-4-1 Conceptual modelling

The reference wind speed, U_a, used in the research is 10 [m/s]. Combined with the chord length of 2.137 meters, this leads to a Reynolds number of around $Re \approx 1.4E6$. Consequently, the flow dynamics are dominated by inertial forces. The Mach number of the flow is around $Ma \approx 0.029$. The fluid can be assumed to be incompressible since $Ma < 0.3$ [2].

The mass in the flow should be conserved, meaning the mass in a specified control volume can not increase or decrease. This physical constraint can be mathematically described by the continuity equation.

$$\frac{\partial \rho}{\partial t} + \vec{u} \cdot \nabla \rho = 0 \tag{3-22}$$

Because the flow is incompressible, density is constant. This reduces the continuity equation to:

$$\nabla \cdot \vec{u} = 0$$

A change in momentum can only be attributed to forces acting on particles or control volumes. This means that for a control volume, such as a bounded flow domain, with no external forces acting on it, the momentum will not change. The conservation of momentum equation can be derived from Newton's second law, and is given in equation 3-23 in differential form for incompressible flow. The first term on the left hand side equals the change in flow velocity over time. The second term on the left hand side is an expression for convection of fluid. The first term on the right hand side is a pressure gradient, the subsequent term is a diffusion term. The last term on the right hand side is the term for external (non-conservative) body forces. Since the equation is derived from Newtons second law, it represents a force balance, and when satisfied, momentum is conserved.

$$\rho \left(\frac{\partial \vec{u}}{\partial t} + (\vec{u} \cdot \nabla)\vec{u} \right) = -\nabla p + \mu \nabla^2 \vec{u} + \rho \vec{f} \tag{3-23}$$

The mass and momentum conservation laws apply on control volumes. Therefore the equations should be applied on a finite flow domain. A square domain is used, of which on each surface a boundary condition is attributed, figure 3-15. The size of the domain is based on the findings in [5]. The inlet is defined as *Inflow* boundary condition and defines the inflow of air, a vector defines the flow velocity in all three Cartesian directions. Uniform inflow conditions will be applied. The outlet and two far-field sides are assigned similar properties. These boundary conditions also specify the turbulence intensity and eddy viscosity in the undisturbed flow. The far-field top surface is defined as *Pressure* boundary condition. The reference pressure is zero, meaning that the pressures in the domain, given in the solution, are the dynamic pressures. Lastly the bottom surface is defined as a *SymmetryPlane* boundary condition, also called a mirror plane. This condition implies that the velocity normal to the surface must be zero, so no fluid can penetrate the surface. However, it is a slip-wall so no boundary layer is generated. All mentioned boundary conditions, except the *Pressure* boundary condition, use Dirichlet condition for momentum and a Neumann condition for pressure. For the *Pressure* condition it is the other way around.

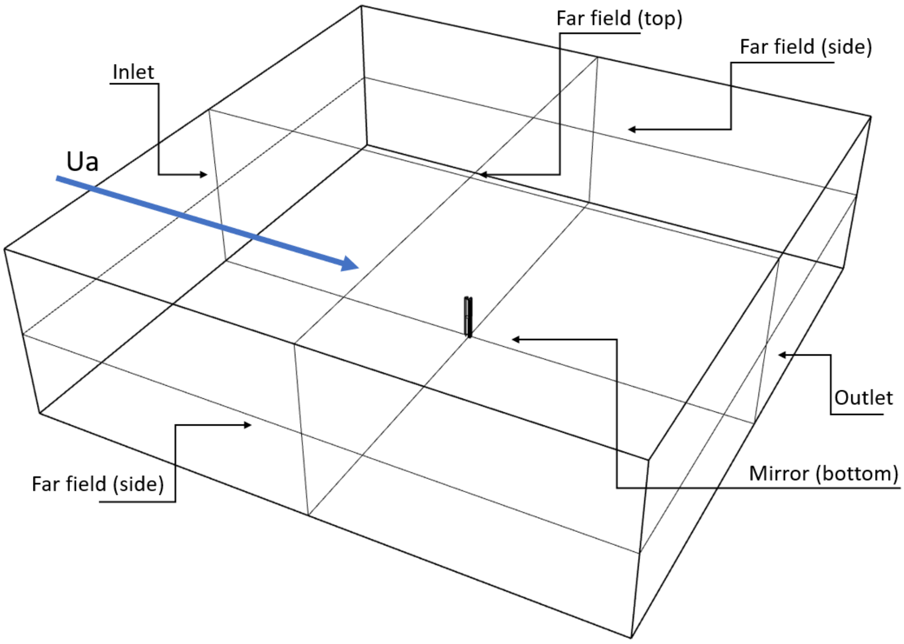

Figure 3-15: Illustration of 3D domain for single Ventifoil RANS simulations

The geometry of the Ventifoil exists of multiple separate surfaces. The suction region exists of 9 slots, of which 5 are suction slots, through which suction is applied, and 4 are closed slots. These are illustrated in yellow in figure 2-9. As can be seen, the slots are not extended to the tip of the Ventifoil. This is done for numerical reasons. Each suction slot is a surface with a pressure condition applied. By assigning a pressure which is lower than the exterior pressure, fluid can flow through the surface, into the interior of the Ventifoil, which then leaves the domain. The pressures needed to obtain appropriate suction coefficients are given in chapter B. The closed suction slots and other surfaces defining the geometry are modelled as *Wall* boundary condition. This no-slip wall leads to the development of a boundary layer.

The conceptual model introduces simplifications which will lead to discrepancies between the model and the reality. For example uniform wind conditions are applied and an Atmospheric Boundary Layer (ABL) is excluded. Additionally the inflow will be steady, while in reality the wind profile is unsteady due to wind gusts. There are also simplifications made in the modelling of the Ventifoil geometry. The suction region is modelled as vertical slots while in practice the suction is applied through small holes. Another example is that the device is modelled on a flat surface without friction instead of on a ship [36].

3-4-2 Mathematical modelling

The first term in the momentum equation is the change in flow momentum over time. For steady flow, this term equals zero. Nonetheless, the flow will be unsteady due to turbulence and (small) vortices shedding of the wing surface. When these effects are assumed small, the solution of the assumed steady flow, can be obtained by applying Reynolds Averaging to the momentum equation. In this modelling assumption, the components of equation 3-23 are averaged over time, leading to the Reynolds Averaged Navier Stokes (RANS) equations for momentum. The time derivative becomes zero but an additional term called the Reynolds stress tensor appears. This term relates to velocity fluctuations. The small scale fluctuations can not be solved on the used grids. Consequently, a turbulence model is needed to approximate this term. From literature it is known that the $k - \omega$ SST turbulence model is appropriate, which will therefore be used [5, 7]. Approximating the momentum equation by applying the RANS equations and using the mentioned turbulence model will introduce representation errors [36].

3-4-3 Numerical modelling

The mass conservation and momentum equations given above are already in differential form. However, both are derived from continues, integral equations. In order to apply the differential equations, the flow domain should also be discretized. Since the time dependent term is removed by applying the RANS equations, only a spatial discretization is needed. The geometry and domain made in Rhinoceros are imported in Hexpress which is grid-meshing software often used by MARIN. The software allows to specify the grid properties in various ways. For each type of simulation structured grids are generated, but the specific grid properties differ slightly for each type of RANS simulation and are therefore briefly discussed in each corresponding chapter. Visual illustrations of the various grids are presented in appendix H.

Extra attention should be given to the grid meshing of the cells in close proximity of the surface of the Ventifoil. Boundary layer dynamics have a large influence on the onset location of flow separation, which in its turn has an influence on the larger scale flow structures and the performance of the device. Furthermore, the boundary layer suction of the Ventifoil is designed to remove the retarded boundary layer flow. This involves small scale flow properties which can not be solved with larger grid cells. For this reason a viscous layer mesh is added to the grid. The size of the first layer of cells directly on the surface is determined by setting a target value for y^+ which is based on friction velocity, u_* and the height of the first cell, y. If the non-dimensional wall distance $y^+ < 5$, the grid cells are located in the viscous sublayer. In this region of the boundary layer, the flow is dominated by viscous stress. Consequently the inertial stress terms can be neglected and the turbulent boundary layer dynamics can be solved. In order to guarantee the viscous sublayer laws are valid, MARIN advises to ensure $y^+ < 1$. This advice is adopted [35].

$$y^+ = \frac{u_* y}{\nu} \tag{3-24}$$

3-4-4 Solver

The differential equations are numerically solved as a system of linear equations, where $\overline{\overline{A}}$ is a matrix of known variables, $\vec{\phi}$ is the vector holding the (unknown) solution of the system and rhs is the right hand side existing of a vector with known variables.

$$\overline{\overline{A}}\,\vec{\phi} = rhs$$

The GMRES method is MARIN standard and used for solving the momentum equation, pressures and turbulence transport. This method tries to minimize the residuals of the solution [43]:

$$\text{Res} = \overline{\overline{A}}\,\vec{\phi} - rhs$$

Since matrix $\overline{\overline{A}}$ is often a large matrix, the solution of the system is found on an iterative manner. Implicit and explicit relaxation factors can be set in order to keep the computations stable. For the discretization of the convection, both for the momentum equation and turbulence transport, a harmonic Total Variation Diminishing (TVD) scheme is used. For RANS simulations TVD schemes are suitable, which are non linear. They eliminate non-physical oscillations which can arise if linear schemes are used [43].

The discretization of governing equations and spatial domain will introduce a discretization error. Other numerical errors are introduced by the convergence tolerance and round-off errors [36]. The size of the discretization error can be approximated by finding the grid independent solution, as is briefly discusses in chapter 3-2-7. A grid refinement study and uncertainty analyses is not performed in this research. This is already done by [5] for similar numerical methods and discretizations also applied on Ventifoil RANS simulations.

3-4-5 Convergence and residuals

The simulation is completed if either the residuals are below the convergence tolerance, or if the maximum iterations are exceeded. Also when the solution diverges to a certain extend, the computation is stopped. The convergence tolerance is set to be $1E-8$. This is expressed in terms of the residuals norm L_2 and L_∞. The residuals are computed in each cell for the velocity in x, y and z direction, for the pressures in the domain, for the transport of turbulent kinetic energy and for the specific rate of dissipation of turbulent kinetic energy. The L_2 norm is computed by taking the root mean square of all the residuals, of one type, in the domain. The L_∞ is a measure for the maximum residual in the domain and is therefore generally higher than L_2. The maximum number of iterations differs per type of RANS simulation.

All settings are defined in a control file which instructs ReFRESCO. Also monitors are added to the control file which can log data such as forces, pressures and velocities. This data can then be used for post-processing. It is also possible to analyse the monitors real-time during the simulation with the use of *Aspect Monitor*. This can help to identify convergent or divergent behavior during the simulation by looking at the residual norms.

For the two dimensional RANS simulations, the maximum numbers of iterations was set to 10000. In figure 3-16a the residual norms in the domain are shown over the iterations. As can be seen, the residuals become stable after around 1500 iterations. Also the force output is converged as shown in figure 3-17. The computational time of each 2D simulation was around $t \approx 15$ minutes by using 320 GB of RAM memory.

Although the residuals in the simulation have converged, the computation still has residuals of the order $1E-3$, which is significantly higher than the convergence tolerance. It is important to know where these residuals are located in the domain. This may reveal locations with bad or insufficient grid quality or locations at the geometry which are computationally challenging.

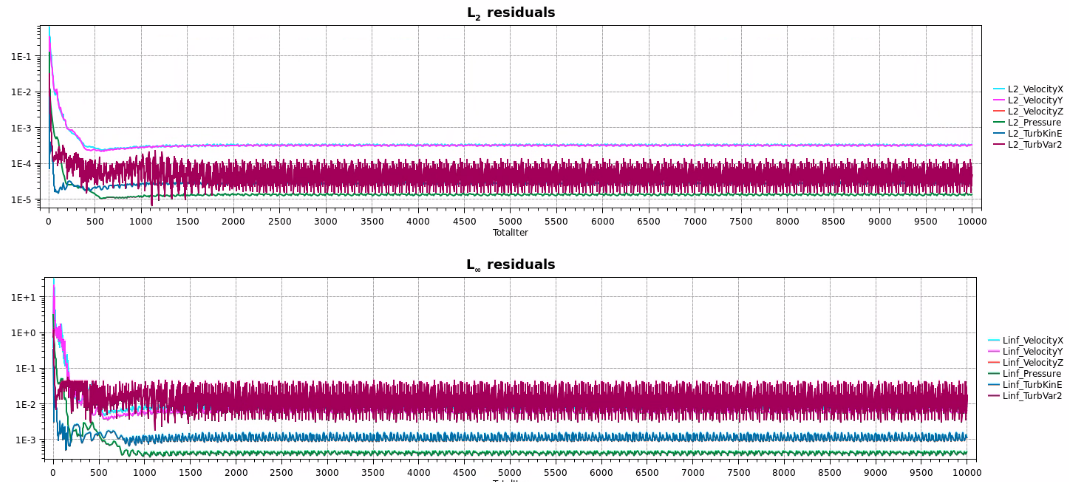

(a) L_2 and L_∞ residuals in 2D domain.

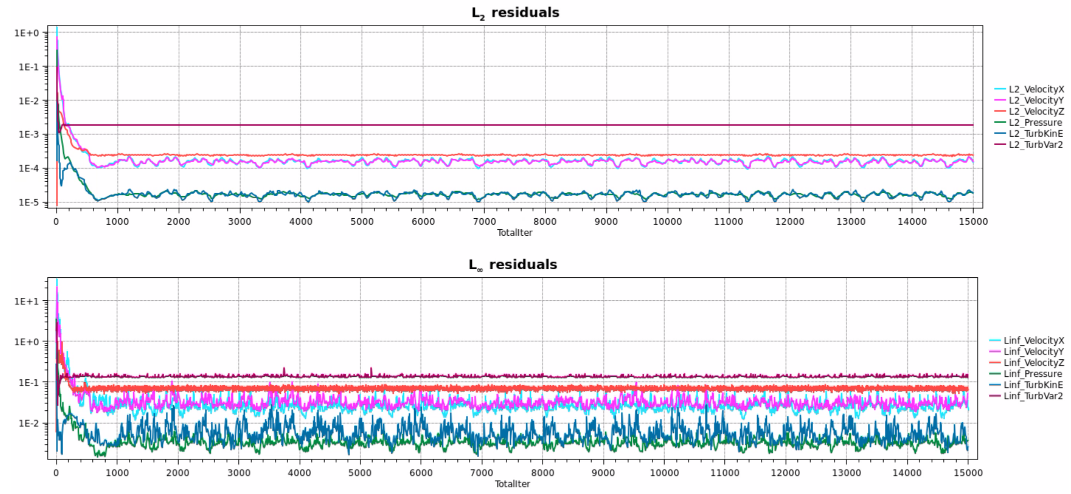

(b) L_2 and L_∞ residuals in 3D domain of single Ventifoil.

Figure 3-16: Residuals in the domain around the Ventifoil at $\alpha_\infty = 25°$.

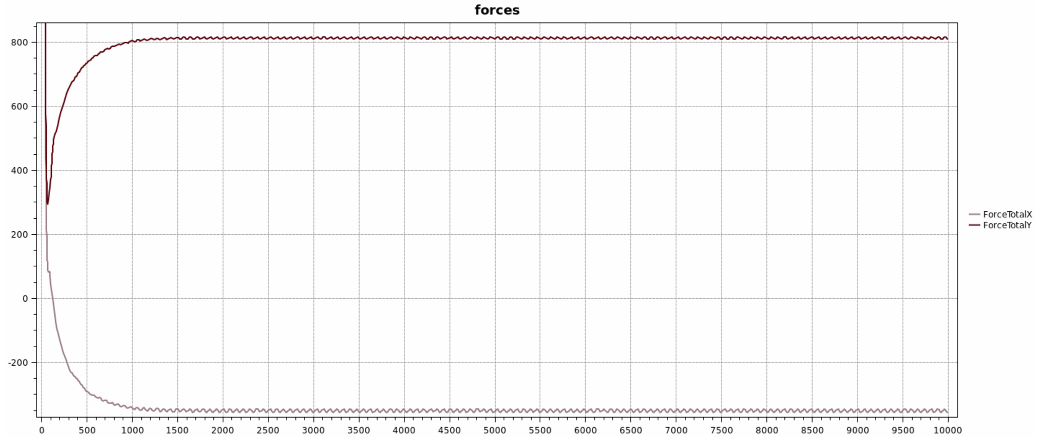

Figure 3-17: Sectional forces in x and y direction at $\alpha_\infty = 25°$.

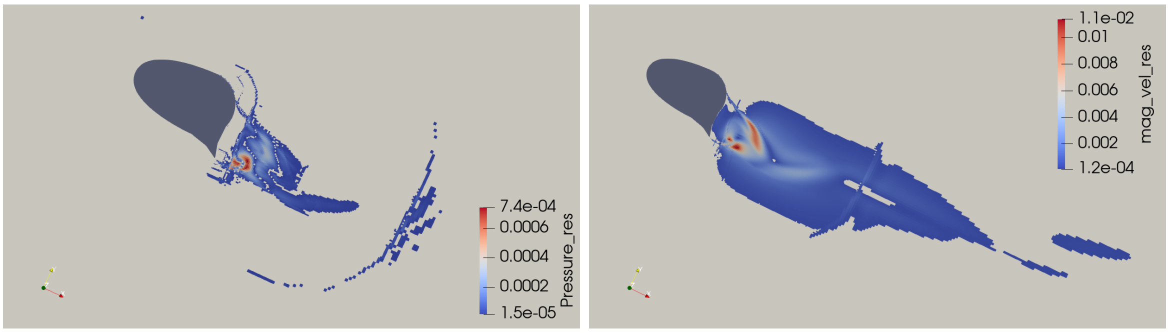

(a) Pressure residuals. **(b)** Velocity residuals.

Figure 3-18: Residuals in the domain around the Ventifoil section at $\alpha_\infty = 25°$.

Table 3-1: Standard deviations in force output of 2D simulations.

α_∞	$\overline{F_x}$	$\overline{F_y}$	$\sigma_{\overline{F_x}} \backslash \overline{F_x}$	$\sigma_{\overline{F_y}} \backslash \overline{F_y}$
$-20°$	59.73	147.11	3.62e-2	1.20e-2
$-10°$	70.89	341.28	5.20e-2	7.86e-3
0°	15.86	425.38	3.26e-1	6.36e-3
5°	-34.66	606.87	-1.64e-1	5.88e-3
10°	-97.43	673.38	-6.16e-2	5.49e-3
15°	-172.66	733.94	-3.42e-2	4.87e-3
20°	-259.54	785.71	-2.00e-2	3.95e-3
25°	-350.19	812.99	-1.14e-2	2.92e-3
30°	-445.81	826.72	-5.14e-3	1.67e-3
35°	-535.73	814.48	-1.64e-3	6.98e-4

Figure 3-18a and 3-18b reveal that the residuals mainly occur in the wake behind the Ventifoil. The pressure residuals occur on the edges between adjacent cells of different sizes. Also the two locations where flow separates from the Ventifoil induce residuals. This is just behind the suction region and at the tip of the flap. In order to further reduce residuals it was decided to apply three sectional grid refinements with varying refinement levels. One was located around the tip of the flap, the other two are located directly behind the Ventifoil overlapping a large part of the wake nearby the Ventifoil. Details on the refinement levels will be given in chapter A. Figure 3-18a and 3-18b show the residuals with the additional sector refinements already implemented.

After convergence of the residuals, the forces still slightly fluctuate in a recurring manner. This can be due to small vortices shedding of the edge of the flap. An example of a 2D force output for $\alpha_\infty = 25°$ is shown in figure 3-17. The extend of the fluctuations in the force output can be expressed in the normalized standard deviation and are given in table 3-1. The normalized standard deviations are small, so solving the flow field as being steady still is valid, confirming the suitability of using RANS equations. The table contains some standard deviations in F_x which are high. This is caused by values of F_x which are close to zero and used as the denominator in the normalization. The aerodynamic coefficients are computed by taking the mean of the final 3000 iterations and equation 2-2.

Table 3-2: Standard deviations in force output of 3D single Ventifoil simulations.

α_∞	$\overline{F_x}$	$\overline{F_y}$	$\sigma_{\overline{F_x}} \backslash \overline{F_x}$	$\sigma_{\overline{F_y}} \backslash \overline{F_y}$
0°	662.13	5319.50	1.5e-4	4.27e-5
5°	306.83	6222.57	3.67e-4	3.27e-5
10°	-172.34	7037.72	-1.14e-3	3.65e-5
15°	-772.19	7753.08	-2.26e-4	6.45e-5
20°	-1467.62	8349.60	-9.06e-4	8.19e-5
25°	-2221.90	8771.14	-1.07e-3	1.74e-4
30°	-2908.42	8829.60	-6.37e-4	1.11e-4
35°	-3468.30	8417.06	-3.75e-3	1.90e-3

The three dimensional RANS simulations for a single Ventifoil were completed in 15000 iterations, because practice showed that instability could occur further on in the iterative process. The computational time of each simulations was round $t \approx 307$ minutes. 384 GB of RAM memory was used. The residuals are mainly located in the wake of the Ventifoil. The residuals of a reference simulation at $\alpha_\infty = 25°$ are shown in figure 3-16b. What can be seen is that the L_2 and L_∞ norm are larger then the residuals in the 2D simulations. This is a common observation for 3D simulations when compared to 2D simulations. The residuals are mainly located in the wake of the Ventifoil. The residuals were tried to be lowered by looking at the grid quality and extra refinement sectors. The grid quality was satisfactory and is further discussed in chapter B-2. The residuals and forces converge after around 1500 iterations. Similar to the two dimensional simulations, there remained some level of fluctuations in the force output. The fluctuations are expressed in terms of the normalized standard deviation and are shown in table 3-2. The forces are obtained by taking the mean of the final 5000 iterations.

For each simulations regarding the double Ventifoil RANS model, 10000 iterations are done. The computational time for each simulation was around $t \approx 147$ minutes, which was faster than the single Ventifoil RANS simulations. For each simulation 768 GB RAM memory was available, which is more computational power than was used for the 3D single Ventifoil simulations. The residuals are of similar order as the residuals in the 3D single Ventifoil simulations. The aerodynamic coefficients are computed based on the mean of the final 5000 iterations and equation 2-2.

Chapter 4

Non-disclosed results

The research scope, questions and method are implemented on the most up-to-date Ventifoil geometry. However, the detailed results are not disclosed since they include sensitive information.

In order to obtain input data for the numerical Lifting Line Model (LLM), first sectional Reynolds Averaged Navier Stokes (RANS) simulations are conducted. The results are presented in confidential appendix A.

The sectional lift and drag curves are subsequently used to obtain three dimensional aerodynamic behavior of a single Ventifoil, by means of the LLM. Also 3D full scale RANS simulations are conducted on a single Ventifoil geometry. The result obtained by both methods are compared and disagree to a certain extend, mainly caused by non-uniform span-wise aerodynamic properties. The results are shown in confidential appendix B.

The LLM is then used to obtain the local conditions, aerodynamic properties and performance of a double Ventifoil configuration. On a subset of conditions, RANS simulations are conducted. Both methods are evaluated on changes in flow direction, flow velocity, pressure field interaction, viscous interaction, and interaction through changes in the suction coefficient. The results are presented in confidential appendix C.

An optimization algorithm is implemented on the LLM for double Ventifoil configurations. This was done in order to maximize the thrust force coefficient. Results are shown in confidential appendix D.

Lastly, in appendix E, G, F and H, detailed figures regarding the thrust force coefficients, pressure distributions, velocity distributions, and grid schematics are given. All of these appendices remain confidential.

Conclusions of the research are disclosed, and presented in chapter 5.

Chapter 5

Conclusions and recommendations

This research started with a background study on Wind Assisted Ship Propulsion (WASP) and the theoretical background of airfoils and Ventifoils. The literature review showed that the presence of multiple devices sharing a flow field would result in significant changes in aerodynamic properties of individual devices. The problem statement resulted in a series of research questions. The main research goal was to evaluate the effect of aerodynamic interaction on aerodynamic performance of two Ventifoils. This chapter will summarize and present the final conclusions of this research. First the results will be discussed. Subsequently, limitations of the results will be discussed and recommendations for further research on the topic will be given.

5-1 Conclusions

In order to evaluate a broad range of environmental and operational conditions, a numerical Lifting Line Model (LLM) is used. First, two dimensional full scale Reynolds Averaged Navier Stokes (RANS) simulations are conducted in order to obtain sectional lift and drag curves. This data functioned as the input data for the LLM. The 2D results obtained by RANS, showed satisfactory agreement with data from literature. This is satisfactory, since the current Ventifoil geometry is slightly different than the devices used in literature. The numerical parameters indicating the grid quality are satisfactory. The suction dynamics, velocity and pressure distributions are as expected. The onset of stall is not included in the sectional lift curve, since the unsteady flow accompanied by this is not appropriately solved with steady RANS. This revealed to be an important limitation of the used method. The suction coefficient for each simulation remained within one percent of the target suction coefficient of $C_q = 0.040$.

The aerodynamics of a single three dimensional Ventifoil is evaluated by means of the numerical LLM and full scale three dimensional RANS simulations. The discretization of the LLM, $N_{cosine} = 10$, resulted in an acceptable discretization error.

The results obtained by the LLM show good agreement with analytical expressions for lift and drag. The span-wise distributions of aerodynamic properties are comparable to span distributions over traditional three dimensional wings. There is no clear onset of stall. It is concluded that this is caused by the absence of stall onset in the input data generated by the 2D RANS simulations.

The results from the RANS method give more insights in the three dimensional properties of the flow and demonstrate that the flow is highly non-uniform over the span of the device. Due to an increasing vertical flow component, the suction coefficient near the tip is much larger than the suction coefficient near the root of the device. The Ventifoil induces significant changes in the flow velocity. Also the up- and downwash showed to be significant.

The results obtained by both methods are compared and show differences in the magnitude of C_L and C_D. The largest discrepancies are found for higher angles of attack, towards the onset of stall in RANS. The non-linearity of the lift curve of the LLM is far less than that of the RANS model due to the absence of stall behavior. Consequently, both curves diverge when α increases. Additionally, it is expected that the overestimation is caused by the LLM assumption of span-wise uniformity. The RANS model allows for a non-uniform distribution of C_q over its span. It is shown that for the largest part of the suction region, C_q is lower than the target value of 0.040. This leads to sectional aerodynamic properties corresponding to lower values of C_l, relative to the input C_l for the LLM, which assumes $C_q = 0.040$ over the each section.

The overestimation of the coefficients by the LLM, for the operational angle of attack, $\alpha_\infty = 25°$, is $\Delta C_L = 7.7\%$ and $\Delta C_D = 11.4\%$.

A benchmark configuration based on two absolute distances $D = 3.5 \cdot c$ and $D = 7 \cdot c$ are evaluated with the LLM over $[0° \leq \beta_a \leq 180°]$. These results are used to answer the research questions.

To what extend does the aerodynamic interaction between two Ventifoils mutually affect aerodynamic performance?

The aerodynamic coefficients from the benchmark configuration are compared with the aerodynamic coefficients of a single Ventifoil. It was concluded that the changes in C_L and C_D are significant for both Ventifoils. Although the change is varying over the apparent wind angle, a general conclusion can be drawn. For a device relatively located downwind, C_L is severely decreased, while C_D is significantly increased. For a device located upwind relative to the other device, C_L is slightly increased and C_D decreased. The changes in aerodynamic coefficients are between $-40\% \leq C_L \leq 6\%$ and $-20\% \leq C_D \leq 65\%$. These numbers match with what is found in literature, presented in paragraph 2-8 and by the definition study in the preamble of this research [9].

The thrust coefficients are decreased over the entire operational domain of the Ventifoil for both absolute distances. The decrease is most severe for $D = 3.5 \cdot c$. For this distance, the aerodynamic interaction leads the a decrease in performance of $\Delta C_X = [-16.3\%, -12.3\%, -3.4\%]$ for upwind, cross wind and downwind conditions respectively. For $D = 7 \cdot c$, the decrease amounts $\Delta C_X = [-9.7\%, -9.0\%, -1.5\%]$ for the same conditions.

Generally it can be concluded that aerodynamic interaction affects the aerodynamic performance to a significant extend. The effect of aerodynamic interaction is most severe for configurations where the Ventifoils are placed parallel to the flow direction. The effect of aerodynamic interaction is also more severe if Ventifoils are placed at smaller absolute distances from each other.

How can the aerodynamic interaction be modelled for practical, adaptive operation and improvement of the aerodynamic performance?

The aerodynamic interaction can be modelled by higher fidelity methods such as the presented 3D RANS method. These methods are valuable to obtain detailed information about the flow field and non-uniformity of parameters over the device. It is concluded that this method does not meet the requirement of being suitable for adaptive operation. This is caused by the computational time needed for the evaluation of one configuration in one environmental condition. There are methods available for reducing the number of simulations necessary to find correlations, but this is outside the scope of this research. The computational time needed for one 3D steady RANS simulation as presented in chapter C amounted up to approximately 150 minutes.

These limitations are not imposed by the LLM, which takes $t < 0.04$ seconds for one evaluation. Additionally, the output allows to conveniently compare the local conditions at each device, with the local conditions of a single Ventifoil. Based on the results obtained by the LLM and RANS simulations, presented in chapter C, it is concluded that the dominant component for the extend of aerodynamic interaction, is the change in effective angle of attack, $\Delta\alpha_e$, which is caused by up- and downwash.

A method focusing on the adaption to the local change in effective angle of attack, is implemented. The objective of the gradient based optimization algorithm is to maximize C_X by independently varying α_∞ of both Ventifoils. The constraint is based on the local conditions occurring at $\alpha_\infty = 30°$, which is the stall angle obtained by the 3D RANS simulations. The constraining local condition at $\alpha_\infty = 30°$ is the maximum value of α_e at the control points of the discretized Ventifoil.

The optimization process leads to an operational guideline instructing α_∞ for both Ventifoils in order to achieve the highest C_X. Based on these guidelines, the thrust coefficient is increased by $\Delta C_X = [+5.3\%, +8.8\%, +10.80\%]$ for $D = 3.5 \cdot c$ and $\Delta C_X = [+6.0\%, +10.1\%, +11.3\%]$ for $D = 7 \cdot c$. Moreover, it is shown that by using the proposed method for adaptive operation, the single Ventifoil can be outperformed in certain environmental conditions in terms of total aerodynamic performance. This was achieved for downwind conditions if $D = 3.5 \cdot c$, and for downwind and cross wind conditions if $D = 7 \cdot c$. This is mainly achieved by adapting the angle of attack of the downwind Ventifoil to downwash.

How are viscous and pressure field interactions involved in overall aerodynamic interaction?

The LLM presented in this research is based on a numerical implementation of the lifting line theory. Consequently, inevitable assumptions and limitations are made. For a subset of the benchmark configuration, full scale three dimensional RANS simulations are conducted. Although the magnitude of C_L and C_D for both methods differ, the results generally follow the trends indicated by the LLM results. In order to validate the LLM, and bypassing the initial difference between the methods found for a single Ventifoil, the reduction ratios of the coefficients are evaluated. In order to evaluate the cause of discrepancies between the resulting reduction ratios, the viscous and pressure field interaction is analysed.

Visual inspection showed that the pressure fields around a single Ventifoil are very different from the pressure field around the Ventifoils in the benchmark configuration. From the figures it could be concluded that if a high pressure side of one device is neighbouring a low pressure side of the other device, the fields were interfering with each other. As a result, the pressures in both regions were mitigated.

In order to approximate the contribution of pressure field interaction to the overall aerodynamic interaction the normalized C_p distributions were evaluated. The typical shape of the distributions made it possible to differentiate pressure field interaction from other interaction components. It was concluded that pressure field interaction has a dominant contribution to overall aerodynamic interaction if opposing pressure fields are facing each other. This happens for configurations were the Ventifoils are positioned transversely to the incoming flow.

The normalized velocity fields around the Ventifoils in the benchmark configuration clearly indicated the decelerated flow region due to the viscous wake of each device. Inspection of the normalized and absolute C_p distributions showed that if a device is located directly in the wake of an upwind located Ventifoil, a large reduction in the suction peak can be expected. When devices are not located near wake fields, the contribution of viscous interaction to overall aerodynamic interaction showed to be insignificant.

It can be motivated that the contribution of pressure field and viscous interaction is dependent on the relative positioning of the devices. The contribution is smaller if the distance between the devices is increased.

What is the effect of aerodynamic interaction on the suction coefficients and subsequently the aerodynamic performance?

The behaviour of ΔC_q was compared to the pressure distributions around the Ventifoils in the benchmark configurations. It was concluded that the change in pressure in the exterior of the Ventifoils suction region, was correlated with the increase or decrease in C_q. Following from this, it was concluded that the pressure field interaction leads to significant changes in the suction coefficient of each device.

In order to evaluate the contribution of ΔC_q to the overall aerodynamic interaction, identical simulations but with a constant $C_q \approx 0.040$ were conducted. From the results it was concluded that a positive ΔC_q resulted in an increase in C_L, while a negative ΔC_q resulted in a decrease in C_L. This is in line with what is known from literature. The result is that ΔC_q has an important mitigating contribution to the total aerodynamic interaction for most of the configurations. The contribution of ΔC_q to the total aerodynamic interaction decreases if the absolute distance between devices is increased.

5-2 Recommendations

This research describes various aspects of aerodynamic interaction between two Ventifoils. Furthermore it uses two methods for modelling the interaction. However, there are of course various ways to improve the research on this subject. This paragraph will give suggestions and recommendations on further research. First recommendations on the numerical LLM will be given. Subsequently advice on improving the implementation of Ventifoils will be given. Lastly some possibilities for future research are discussed.

Recommendations on the numerical LLM

The current numerical algorithm makes it difficult to differentiate self induced changes in local conditions from changes in local conditions induced by other devices. It would be useful to separate these factors. This might lead to better understanding of, and adaption to, the aerodynamic interaction between multiple devices. This may be done by writing a code which can differentiate the contributions of different devices to the total vortex matrix.

The three dimensional RANS simulations revealed large non-uniformity regarding the distribution of C_q over the span of the device. It was motivated that this might cause discrepancies between the aerodynamic properties of single Ventifoil modelled by the LLM and RANS simulations. It would be interesting to add a possibility to vary C_q over the span of the device in the lifting line algorithm. This could be done by attributing different sectional properties to each discretized segment of the LLM. The different sectional properties can then be based on the estimated or average C_q at that specific section. This way sectional properties corresponding to lower values of C_q can be attributed on the lower part of the Ventifoil. Sectional data corresponding to a higher C_q can be used as input for segments more closer to the tip of the Ventifoil.

The current model is limited to the assessment of potential flow effects. It was concluded that the pressure field interactions can have a significant contribution to overall aerodynamic interaction. It would be interesting to include a, possibly empirical, correction method for pressure field effects.

Recommendations on the presented implementation of the LLM

The implementation of the LLM is in this research not accurate in estimating lift and drag coefficients for higher angles of attack. The onset of stall is not clearly indicated because this is also not incorporated in the sectional lift and drag curves. Because of this, the adaptive operation can not be constrained based on the stall conditions, which would be favorable. In order to improve the computations for lift and drag at higher angles of attack, it is advised to perform two dimensional unsteady RANS simulations for $\alpha = [30, 35, 40, 45]$ degrees and include this in the input of the LLM.

The optimization algorithm leading to the adaptive operation only has α_∞ of both Ventifoils as design variables. Nonetheless, the Ventifoil also has the possibility to vary flap angle and C_q during operation. It is advised to expand the database of sectional aerodynamic coefficients, with input for a variety of flap angles and suction coefficients. This can be obtained by similar 2D RANS simulations. Based on the expanded data set, and a more advanced optimization algorithm with multiple design variables, the LLM should be able to generate more sophisticated adaptive operational guidelines for the Ventifoils. A research presented by [34] shows that increasing the flap angle of a downwind device can potentially mitigate the detrimental effects of aerodynamic interaction.

The implementation of the LLM in this thesis is limited to uniform inflow conditions. However, this condition is a very poor representation of realistic flow conditions. Wind at sea actually has a vertical gradient which leads to a span-wise variation of wind speed and flow angle. Additionally, global probability on the occurrence of true wind speeds can be combined with average ship velocities to obtain a probability distribution of the apparent wind speed. It would be interesting to see the effect of these more complex inflow and environmental conditions on aerodynamic performance and adaptive operational guidelines.

In this research it is decided to evaluate interaction effects and its effect on aerodynamic coefficients based on the change in effective angle of attack, and local flow velocity. Maritime Research Institute Netherlands (MARIN) has used a different method on the interaction of Flettner Rotors, which is referred to as the effective wind method. It would be interesting to implement this method on Ventifoil interaction.

The current study uses two benchmark configurations to evaluate aerodynamic interaction. It is recommended to expand the number of configurations with setups existing of three, four or more Ventifoils. This could be of value to actual on-board configurations implemented by Econowind.

Recommendations on future research

If it is desired to evaluate aerodynamic interaction on a large set of conditions, but with more fidelity than obtained by the LLM, there is an alternative approach. Design Of Experiments is a method which enables the exploration of large multi dimensional design spaces, such as the problem addressed in this research, with a limited amount of evaluations. This allows to use the more computationally heavy three dimensional RANS method on a statistically selected set of design combinations. The results following from the set of simulations can then be used in a regression analyses on the coherence of the design variables and aerodynamic coefficients. Moreover, this approach can be used to further validate the LLM. This is shown to be a valuable method in the research of [32]. Also machine learning methods can potentially be used to find correlations between a limited set of design combinations and aerodynamic properties.

Because of the physical foundations and the proposed method for modelling this, Ventifoils are interchangeable with other WASP devices. It can be interesting to apply a similar approach as what is presented in this thesis on different wind propulsion devices.

Lastly it is advisable to validate the findings presented in this thesis with on-board experiments. An approach as discussed in chapter D-4 can be used as guideline.

Bibliography

[1] IMO and MEPC.1/Circ.855/Rev.2, “Guidelines on Survey and Certification of the energy efficiency index,” tech. rep., 2019.

[2] P. Kundu, *Fluid Mechanics - Sixth Edition.* 2012.

[3] B. Charrier, J. Constans, J. Y. Cousteau, A. Daïf, L. Malavard, and J. L. Quinio, “Fondation Cousteau and windship propulsion 1980 - 1985 system Cousteau - Pechiney,” *Journal of Wind Engineering and Industrial Aerodynamics*, vol. 20, no. 1-3, pp. 39–60, 1985.

[4] L. Malavard, “Un nouveau propulseur eolien de navire,”

[5] L. Lagendijk, “Performance investigation of VentiFoil ship propulsion,” 2018.

[6] K. Graf, A. V. Hoeve, and S. Watin, “Comparison of full 3D-RANS simulations with 2D-RANS/lifting line method calculations for the flow analysis of rigid wings for high performance multihulls,” *Ocean Engineering*, vol. 90, pp. 49–61, 2014.

[7] A. Kisjes and E. Committee, “Assesing the Performance of a VentiFoil for Wind Assisted Propulsion,” p. 113, 2017.

[8] R. Stengel, “Aircraft Flight Dynamics - Low Speed Aerodynamics - MAE331 - Lecture slights,” 2018.

[9] M. Borren, “The assessment of aerodynamic interaction for Wind Assisted Ship Propulsion,” tech. rep., 2021.

[10] T. M. Faure, L. Hétru, and O. Montagnier, “Aerodynamic features of a two-airfoil arrangement,” *Experiments in Fluids*, vol. 58, no. 10, 2017.

[11] G. Bordogna, *Aerodynamics of wind assisted ships.* 2020.

[12] J. Winslow, H. Otsuka, B. Govindarajan, and I. Chopra, “Basic understanding of airfoil characteristics at low Reynolds numbers (104–105),” *Journal of Aircraft*, vol. 55, no. 3, pp. 1050–1061, 2018.

[13] M. Garenaux, “Numerical Analysis of Flettner Rotors Performances on the MARIN Hybrid Transition Coaster,” no. 2012, pp. 297–313, 2019.

[14] A. Persson, D. Q. Li, F. Olsson, S. Werner, and U. Dhomé, "Performance prediction of wind propulsion systems using 3D CFD and route simulation," *RINA, Royal Institution of Naval Architects - International Conference on Wind Propulsion, WP 2019*, no. October, pp. 19–30, 2019.

[15] L. Jones, M. Prince, D. Hudson, and J. Cocks, "Predicted fuel-savings for a flettner rotor assisted tanker using computational fluid dynamics," *RINA, Royal Institution of Naval Architects - International Conference on Wind Propulsion, WP 2019*, no. October, pp. 9–18, 2019.

[16] T. Nakashima, Y. Yamashita, Y. Nihei, and Q. Li, "A basic study for propulsive performance prediction of a cascade of wing sails considering their aerodynamic interaction," *Proceedings of the International Offshore and Polar Engineering Conference*, vol. 8, pp. 995–1001, 2011.

[17] F. Tillig, *Simulation model of a ship's energy performance and transportation costs.* 2020.

[18] K. Malmek, U. Dhome, L. Larsson, S. Werner, J. Ringsberg, and C. Finnsgard, "Comparison of Two Rapid Numerical Methods for Predicting the Performance of Multiple Rigid Wing-Sails," *Innovsail*, p. 10, 2020.

[19] J. F. Wellicome, "Some comments on the relative merits of various wind propulsion devices," *Journal of Wind Engineering and Industrial Aerodynamics*, vol. 20, no. 1-3, pp. 111–142, 1985.

[20] IMO and MEPC, "Fourth IMO Greenhouse Gas Study," Tech. Rep. 11, 2021.

[21] IMO and MEPC, "Initial IMO strategy on reduction of GHG emissions from ships," tech. rep., 2018.

[22] IMO and MEPC.1/Circ.815, "Guidance for the treatment of innovative energy efficiency technologies in calculation and verification of the attained EEDI," tech. rep., 2013.

[23] S. Kumar and S. Narayanan, "Airfoil thickness effects on flow and acoustic characteristics," *Alexandria Engineering Journal*, vol. 61, no. 6, pp. 4679–4699, 2021.

[24] J. Anderson, *Fundamentals of Aerodynamics*, vol. 48. 1991.

[25] I. Abbott and A. von Doenhoff, *Theory of wing sections.* 1958.

[26] R. Eppler, "Airfoils with boundary layer suction, design and off-design cases," *Aerospace Science and Technology*, vol. 3, no. 7, pp. 403–415, 1999.

[27] N. J. van der Kolk, *Sailing Efficiency and Course Keeping Ability of Wind Assisted Ships.* 2020.

[28] F. Garzón and A. Figueroa, "The Study on the Flow Generated by an Array of Four Flettner Rotors: Theory and Experiment," *Applied Mathematics*, vol. 08, no. 12, pp. 1851–1858, 2017.

[29] T. Fujiwara, G. E. Hearn, F. Kitamura, and M. Ueno, "Sail-sail and sail-hull interaction effects of hybrid-sail assisted bulk carrier," *Journal of Marine Science and Technology*, vol. 10, no. 2, pp. 82–95, 2005.

[30] K. Ouchi, K. Uzawa, A. Kanai, and M. Katori, “Wind Challenger the Next Generation Hybrid Sailing Vessel,” *International Symposium on Marine Propulsors*, no. May, pp. 562–567, 2013.

[31] Q. Li, Y. Nihei, T. Nakashima, and Y. Ikeda, “A study on the performance of cascade hard sails and sail-equipped vessels,” *Ocean Engineering*, vol. 98, pp. 23–31, 2015.

[32] J. Fu, S. Ji, and X. Huang, “The Effects of Design Parameters on Tandem-Airfoil configuration Aerodynamics,” *School of Aerospace Engineering Beijing*, 2016.

[33] B. Wagner, “Windkanalversuche für einen sechsmastigen Segler nach Prölss,” no. 173, 1967.

[34] H. Lee, Y. Jo, D. J. Lee, and S. Choi, “Surrogate model based design optimization of multiple wing sails considering flow interaction effect,” *Ocean Engineering*, vol. 121, pp. 422–436, 2016.

[35] F. T. Nieuwstadt, B. J. Boersma, and J. Westerweel, *Turbulence: Introduction to theory and applications of turbulent flows.* 2016.

[36] L. Larsson and H. C. Raven, *Principles of Naval Architecture Series - Ship Resistance and Flow.* Society of Naval Architects and Marine Engineers, 2010.

[37] D. Tam, “Advanced Fluid Dynamics - 45042 - Lecture slides,” 2020.

[38] A. Gentry, “The Aerodynamics of Sail Interaction,” *Third AIAA Symposium of AeroHydrodnautics of Sailing*, pp. 1–12, 1971.

[39] J. T. Reid and D. F. Hunsaker, “A general approach to lifting-line theory, applied to wings with sweep,” tech. rep., 2020.

[40] W. F. Phillips and D. O. Snyder, “Modern adaptation of Prandtl’s classic lifting-line theory,” *Journal of Aircraft*, vol. 37, no. 4, pp. 662–670, 2000.

[41] L. Eça and M. Hoekstra, “A procedure for the estimation of the numerical uncertainty of CFD calculations based on grid refinement studies,” *Journal of Computational Physics*, vol. 262, pp. 104–130, 2014.

[42] H. Soeding, “Prediction of Ship Steering Capabilities.,” *Schiffstechnik*, vol. 29, no. 1, pp. 3–29, 1982.

[43] M. Pourquie and R. Pecnik, “Modeling of thermo- and fluid dynamic systems - ME45155 - Lecture slides,” 2021.

Glossary

List of Acronyms

MARIN	Maritime Research Institute Netherlands
WASP	Wind Assisted Ship Propulsion
CFD	Computational Fluid Dynamics
LL	Lifting Line
LLM	Lifting Line Model
IMO	International Maritime Organization
MEPC	Maritime Environment Protection Committee
GHG	Green House Gas
EEDI	Energy Efficiency Design Index
DOE	Design Of Experiments
ABL	Atmospheric Boundary Layer
RANS	Reynolds Averaged Navier Stokes
URANS	Unsteady Reynolds Averaged Navier Stokes
LES	Large Eddy Simulations

List of Symbols

α_∞ [°]	Undisturbed angle of attack
α_e [°]	Effective angle of attack
α_i [°]	Induced angle of attack
β_a [°]	Apparent wind angle
β_t [°]	True wind angle
β_{flap} [°]	Flap angle
Δ	Indicating a change or difference between two parameters
δ [°]	Sheet angle
Γ $[\frac{m^2}{s}]$	Circulation
λ [°]	Drift angle - difference between steered coarse and actual coarse of ship
λ_T [-]	Thickness ratio

$\overline{\alpha_e}$ [°]	Mean effective angle of attack over span
$\overline{U_{loc}}$ [$\frac{m}{s}$]	Mean local flow velocity over span
θ [°]	Angle of suction region
θ_m [°]	Mid angle of suction region
ε [-]	Aerodynamic efficiency - ratio between lift and drag coefficients
$\vec{U}(\vec{x})$ [$\frac{m}{s}$]	Velocity vector in point (x, y, z)
AR [-]	Ratio between span and cord length
AR_e [-]	Ratio between effective span and cord length
c [m]	Chord length
C_D [-]	Three dimensional drag coefficient
C_d [-]	Two dimensional drag coefficient
C_L [-]	Three dimensional lift coefficient
C_l [-]	Two dimensional lift coefficient
C_p [-]	Pressure coefficient
C_q [-]	Suction coefficient
D [m]	Distance between Ventifoils
F_D [N]	Drag force
F_L [N]	Lift force
F_T [N]	Total force on airfoil
G [-]	Non-dimensional circulation
L_2	Root mean square of all residuals in domain
L_∞	Highest residual in domain
P_a [kW]	Aspiration power
p_{suc} [Pa]	Pressure imposed in the boundary condition of the suction slots.
s [m]	Airfoil span height
t [m]	Thickness
u_* [$\frac{m}{s}$]	Friction velocity
U_a [$\frac{m}{s}$]	Apparent wind velocity
U_t [$\frac{m}{s}$]	True wind velocity
U_{loc} [$\frac{m}{s}$]	Local flow velocity
V_i [$\frac{m}{s}$]	Induced velocity
V_s [$\frac{m}{s}$]	Ship velocity
y^+ [-]	Non-dimensional wall distance
A [m]	Planform area
w [$\frac{m}{s}$]	Downwash